

PAPER • OPEN ACCESS

Ion temperature clamping in Wendelstein 7-X electron cyclotron heated plasmas

To cite this article: M.N.A. Beurskens *et al* 2021 *Nucl. Fusion* **61** 116072

View the [article online](#) for updates and enhancements.

You may also like

- [Confinement in electron heated plasmas in Wendelstein 7-X and ASDEX Upgrade: the necessity to control turbulent transport](#)
M.N.A. Beurskens, C. Angioni, S. A. Bozhenkov *et al.*
- [Microinstabilities in hydrogen- and helium-dominated multi-ion-species plasmas in LHD](#)
Masanori Nunami, Motoki Nakata, Hideo Sugama *et al.*
- [Characteristics of electron temperature profile stiffness in electron-heated plasmas on EAST](#)
J.W. Liu, Q. Zang, Y. Liang *et al.*

Ion temperature clamping in Wendelstein 7-X electron cyclotron heated plasmas

M.N.A. Beurskens^{1,*}, S.A. Bozhenkov¹, O. Ford¹, P. Xanthopoulos¹,
A. Zocco¹, Y. Turkin¹, A. Alonso², C. Beidler¹, I. Calvo²,
D. Carralero², T. Estrada², G. Fuchert¹, O. Grulke^{1,5}, M. Hirsch¹, K. Ida³,
M. Jakubowski¹, C. Killer¹, M. Krychowiak¹, S. Kwak¹, S. Lazerson¹,
A. Langenberg¹, R. Lunsford⁴, N. Pablant⁴, E. Pasch¹, A. Pavone¹,
F. Reimold¹, Th. Romba¹, A. von Stechow¹, H.M. Smith¹, T. Windisch¹,
M. Yoshinuma³, D. Zhang¹, R.C. Wolf¹ and the W7-X Team^{1,a}

¹ Max-Planck Institute for Plasma Physics, 17491 Greifswald, Germany

² Laboratorio Nacional de Fusión, CIEMAT, 28040 Madrid, Spain

³ National Institute for Fusion Science, National Institutes of Natural Sciences, Toki 509-5292, Japan

⁴ Princeton Plasma Physics Laboratory, Princeton, NJ 08543, United States of America

⁵ Technical University of Denmark, Kongens Lyngby 2800, Denmark

E-mail: Marc.Beurskens@ipp.mpg.de

Received 30 April 2021, revised 30 June 2021

Accepted for publication 20 July 2021

Published 25 October 2021



CrossMark

Abstract

The neoclassical transport optimization of the Wendelstein 7-X stellarator has not resulted in the predicted high energy confinement of gas fueled electron-cyclotron-resonance-heated (ECRH) plasmas as modelled in (Turkin *et al* 2011 *Phys. Plasmas* 18 022505) due to high levels of turbulent heat transport observed in the experiments. The electron-turbulent-heat transport appears non-stiff and is of the electron temperature gradient (ETG)/ion temperature gradient (ITG) type (Weir *et al* 2021 *Nucl. Fusion* 61 056001). As a result, the electron temperature T_e can be varied freely from 1 keV–10 keV within the range of $P_{\text{ECRH}} = 1\text{--}7$ MW, with electron density n_e values from $0.1\text{--}1.5 \times 10^{20} \text{ m}^{-3}$. By contrast, in combination with the broad electron-to-ion energy-exchange heating profile in ECRH plasmas, ion-turbulent-heat transport leads to clamping of the central ion temperature at $T_i \sim 1.5 \text{ keV} \pm 0.2 \text{ keV}$. In a dedicated ECRH power scan at a constant density of $\langle n_e \rangle = 7 \times 10^{19} \text{ m}^{-3}$, an apparent ‘negative ion temperature profile stiffness’ was found in the central plasma for ($r/a < 0.5$), in which the normalized gradient $\nabla T_i/T_i$ decreases with increasing ion heat flux. The experiment was conducted in helium, which has a higher radiative density limit compared to hydrogen, allowing a broader power scan. This ‘negative stiffness’ is due to a strong exacerbation of turbulent transport with an increasing ratio of T_e/T_i in this electron-heated plasma. This finding is consistent with electrostatic microinstabilities, such as ITG-driven turbulence. Theoretical calculations made by both linear and nonlinear gyro-kinetic simulations performed by the GENE code in the W7-X three-dimensional geometry show a strong enhancement of turbulence with an increasing ratio of T_e/T_i . The exacerbation of turbulence with increasing T_e/T_i is also found in tokamaks and inherently enhances ion heat transport in electron-heated

* Author to whom any correspondence should be addressed.

^a See Klinger *et al* 2019 (<https://doi.org/10.1088/1741-4326/ab03a7>) for the W7-X Team.



Original content from this work may be used under the terms of the [Creative Commons Attribution 3.0 licence](https://creativecommons.org/licenses/by/3.0/). Any further distribution of this work must maintain attribution to the author(s) and the title of the work, journal citation and DOI.

plasmas. This finding strongly affects the prospects of future high-performance gas-fueled ECRH scenarios in W7-X and imposes a requirement for turbulence-suppression techniques.

Keywords: turbulent transport, electron heated plasmas, ion heat transport, neoclassically optimised stellarator, power balance, profile stiffness, ion temperature clamping, Electron cyclotron heating

(Some figures may appear in colour only in the online journal)

1. Introduction

The Wendelstein 7-X (W7-X) experiment [1–3] is a stellarator with predicted good equilibrium properties and high normalized pressures of up to $\langle\beta\rangle \sim 5\%$. Its three-dimensional magnetic configuration has been optimized such that neoclassical transport losses due to finite magnetic ripples have been minimized. For the reactor's relevant low-collisionality $1/\nu$ and $\sqrt{\nu}$ transport regimes, the neoclassical transport scales according to:

$$\chi_{1/\nu} = \varepsilon_{\text{eff}}^{3/2} \cdot \frac{T^{7/2}}{n \cdot R_0^2 \cdot B_0^2} \quad (1.1)$$

and

$$\chi_{\sqrt{\nu}} = \sqrt{n} \cdot T^{5/4} \cdot \left(\frac{r}{E_r}\right)^{3/2} \quad (1.2)$$

[4]. Here, n and T represent the species density and temperature, respectively. The reduction of the effective magnetic ripple $\varepsilon_{\text{eff}} < 1\%$ in W7-X has minimized the neoclassical transport losses in the reactor relevant $1/\nu$ regime. This neoclassical transport optimization has been experimentally demonstrated in plasmas in which the turbulent heat transport is suppressed by means of steep density gradients. Thanks to the beneficial 3D geometry of W7-X [5], both the ion temperature gradient (ITG) and trapped-electron-mode (TEM) turbulence may be reduced or even suppressed when the ion temperature and density gradients align [6, 7] and the (ion) neoclassical transport becomes the more dominant transport mechanism. These conditions were achieved after a train of ice pellets transiently produced a peaked density profile. In these plasmas a central ion temperature of more than $T_{i,0} = 3$ keV could be achieved at a central density of $n_{e,0} = 8 \times 10^{19} \text{ m}^{-3}$, with hydrogen as a fuel and with only 5 MW of electron cyclotron resonance heating (ECRH) [8–10]. The improved confinement was lost after relaxation of the density profile over a particle-confinement timescale of several 100 ms, and oftentimes due to an MHD event [8]. Despite this transient nature, neoclassical transport simulations have shown that this high performance would not have been possible in a neoclassically less-optimized stellarator [8, 10, 11] and hence, the neoclassical optimization of W7-X was demonstrated. The energy confinement scaling of the most successful plasmas is 40% larger than given by the International Stellarator Confinement Scaling ISS04 [12, 13].

This paper discusses a transport regime in which turbulent transport is not suppressed, and the performance is limited with respect to the ISS04 scaling. So far, this has been the case for almost all stationary plasmas in W7-X with ECRH heating and standard divertor- or main-chamber gas fueling. These

plasmas feature flat density profiles, and their transport is dominated by anomalous transport. Their confinement scaling lies at or is less than the ISS04 scaling, depending on the density in these plasmas [14]. At low densities, the confinement timescales are similar to the ISS04 scaling i.e. $\tau_{E,\text{ISS04}} \sim n^{0.51}$, whereas, at high densities that approach the radiative density limit, an increase in density no longer scales beneficially following $\tau_E \sim n^\alpha$, with $\alpha \approx 0$. Beyond the radiative density limit, increasing the density further becomes detrimental and $\alpha < 0$. The decrease of α with density is gradual rather than abrupt, such that for almost the entire accessible density range, increasing the density leads to an increase in the stored energy [14]. Typically, in such plasmas, a radiative front is held outside the normalized minor radius of $r/a \sim 0.8$ until the radiative density limit is reached, as shown in appendix A. In the confinement region $r/a < 0.8$ the radiation losses are very small indeed and well below the 5% level of the ECRH input power. Indeed turbulent transport, and not radiation losses, limit the heat transport and are responsible for the so-called ion temperature clamping observed in these plasmas.

The maximum line-averaged density achieved so-far in W7-X in a gas-fueled ECRH heated plasma is $\langle n_e \rangle = 1.4 \times 10^{20} \text{ m}^{-3}$ with $P_{\text{ECRH}} = 6$ MW and second-harmonic ordinary resonance heating (140 GHz, $B = 2.5$ T) in a plasma with a low impurity content ($Z_{\text{eff}} \sim 1.3$) following boronization wall conditioning [15], although its confinement scaling was low at $\tau_E/\tau_{E,\text{ISS04}} \sim 0.6$ ($\tau_E = W_{\text{dia}}/P_{\text{tot}}$, where P_{tot} is the total input power). Nevertheless, such plasmas are impressively stationary, with the longest high-power pulse ($P_{\text{ECRH}} = 5$ MW) and detached divertor conditions lasting for 30 s [16, 17]. At a lower input power $P_{\text{ECRH}} = 2$ MW, and under attached divertor conditions, a pulse length of 100 s was even achieved [2, 18].

The density profiles in such plasmas are flat to slightly peaked, as can be seen from e.g. the density profiles shown in this paper. Based on the assumption that neoclassical transport is the dominant transport process, the fear was expressed in [19], that hollow density profiles are inevitable in W7-X centrally heated plasmas, given the recycling properties of the device. However, in actual experiments, no evidence of hollow electron density profiles has been found, indicating that turbulent rather than neoclassical transport may dominate the particle transport. This has been confirmed by impurity transport experiments. In [20] no Z -dependence of the impurity transport was observed, although it had been expected, based on neoclassical transport predictions. Moreover, in an ECRH experiment at low electron density, it was shown that the impurity transport time (τ_{imp}) lies well below its neoclassical

prediction [21], and no sign of impurity accumulation was seen. Furthermore, in a follow-up ECRH power-step-down experiment, it was shown that τ_{imp} decreases with an increase of the ratio of T_e/T_i when P_{ECRH} is increased [22]. The latter is a signature of ITG-type turbulence, and the experimental findings are consistent with linear turbulence calculations using the GENE code [23] (as will be shown in this paper).

Now turning to the heat transport, the electron temperature in gas-fueled ECRH plasmas can be varied widely from ~ 1 to 10 keV, depending on density and input power, as seen in figure 1. At low electron densities in W7-X with central electron root confinement, neoclassical transport contributes significantly to the total power balance (PB), as was reported in [24–26]. However, at increasing densities, it was shown that the electron heat transport is dominated by turbulence, in which the electron heat diffusivity $\chi_{\text{turb,e}}$ is larger than the neoclassical diffusivity by up to an order of magnitude. PB analysis shows that $\chi_{\text{turb,e}} = \chi_{\text{PB,e}} = 0.6 \pm 0.2 \text{ m}^2 \text{ s}^{-1}$, with only a small dependence on the magnetic configuration [27], and no clear sign of a critical normalized electron temperature gradient $(a \cdot \frac{\nabla T_e}{T_e})_{\text{crit}} = a/L_{T_e, \text{crit}}$ or threshold. In [27] it is therefore concluded that the electron turbulent transport is largely diffusive. In the same work, heat pulse propagation (HPP) studies showed that the electron turbulent transport is likely driven by ETG and/or ITG turbulence in the core with, indeed, a small degree of electron transport stiffness with $\chi_{\text{HPP,e}}/\chi_{\text{PB,e}} < 2$.

The ion heat transport in stationary gas-fueled plasmas with ECRH heating is the subject of this publication. Already noted in [8] is the fact that the ion temperature in gas-fueled ECRH plasmas is saturated or ‘clamped’ at $T_i \sim 1.5 \pm 0.2 \text{ keV}$, as seen in figure 1. Counter to the post-pellet plasmas in [8], in which $T_i > 3 \text{ keV}$ was transiently achieved, the clamping of T_i appears virtually irrespective of the applied ECRH power and the electron density and electron temperature values obtained. Moreover, all of these plasmas feature flat to slightly peaked density profiles and therefore no density-gradient-aided turbulence suppression. Figure 1 shows that virtually the same $T_i \sim 1.5 \pm 0.2 \text{ keV}$ is achieved in four configurations with various degrees of neoclassical optimization, where one would expect a clear separation on the basis of neoclassical simulations between low and high ε_{eff} configurations, as shown by the grey symbols in the figure. The details of the configurations are given in table 1. The neoclassical transport simulations were conducted with the Neoclassical-Transport-Solver -Suite (NTSS) using mono-energetic transport coefficients for both configurations as calculated using the Drift Kinetic Equation Solver (DKES) as in [28, 29]. For the simulations, a wide range of densities with flat density profiles, and a for W7-X representative centrally deposited ECRH heating with $P_{\text{ECRH}} = 4.5 \text{ MW}$ are assumed. It should be noted that in addition to the configuration insensitivity, the clamped central T_i found in the experiments lies well below the neoclassical predictions; another indication that different types of transport are at play.

The question arises as to why the electron-heated plasmas feature this clamped central ion temperature. Is the central

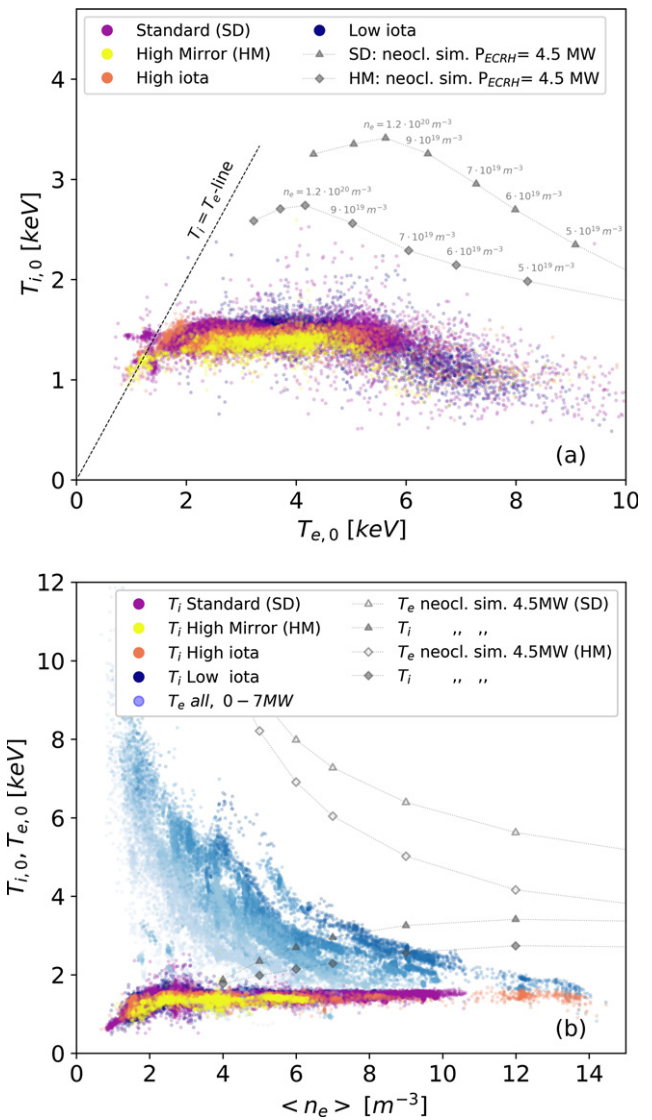








Figure 1. Clamping of the ion temperature T_i in gas-fueled, ECRH heated plasmas in four configurations with varying magnetic ripples (see table 1 for a description of the configurations) as a function of (a) electron temperature T_e , (b) line averaged density $\langle n_e \rangle$. Also shown in (a) and (b) are the neoclassical simulations for $P_{\text{ECRH}} = 4.5 \text{ MW}$ for the ‘standard’ (grey triangles) and ‘high mirror’ configurations (grey squares). In these simulations, the highest temperatures can be achieved in the standard configuration (T_i filled, and T_e open symbols), thanks to its better neoclassical optimization and smaller effective magnetic ripple (ε_{eff}).

temperature limited simply because the heat per particle transferred to the ions does not increase with an increase in the density or heating power? Or is it caused by the off-axis nature of the exchange power, so that no heat arrives at the core of the plasma? Or rather, does turbulent transport limit the ion temperature gradients, and is the clamping related to profile stiffness? As an answer to these questions, it will be shown in this paper that the T_i clamping is the result of a combination of effects: (a) the limited and broad ion heating due to power transfer from electrons in ECRH heated plasmas, (b) the expected increase of heat transport according to the gyro-Bohm scaling and (c) the exacerbated turbulent heat

Table 1. Details of the magnetic configurations.

Configuration	Symbols in figure 1		Effective magnetic ripple $\langle \varepsilon_{\text{eff}} \rangle$ (%)	Boundary ι (divertor geometry)
	Experimental	Neoclassical		
Standard			0.8	5/5
High mirror			2.5	5/5
High iota		—	0.85	5/4
Low iota		—	1.5	5/6

transport due to the effect of an increasing T_e/T_i ratio on ITG turbulence in such plasmas. The rest of this paper will address each of these aspects in turn, giving the full details of the simulations and experiments used to reach this conclusion.

2. Ion heating in ECRH plasmas

In order to select the target experimental conditions for the ion heat transport study, we first look at the variation of the ion heating profiles under typical experimental conditions. In electron-heated plasmas, the ions are heated indirectly through the electron-to-ion exchange power p_{e-i} , which for illustration purposes for a single-species plasma (where $n_e = n_i \cdot Z$), and following [30], is given by:

$$p_{e-i} = \frac{3}{2} \cdot \frac{q_e \cdot n_e \cdot 10^{19} \cdot (T_e - T_i)}{\tau_{ei}} \approx 38 \cdot n_e^2 \cdot \frac{(T_e - T_i)}{T_e^{3/2}} \cdot \frac{Z}{M} \text{ (kW m}^{-3}\text{)} \quad (2.1)$$

$$\tau_{ei} = \frac{M \cdot m_p}{m_e} \cdot \tau_{ee} \approx \frac{M}{Z^2 \cdot \Lambda_{ee}} \cdot \frac{T_e^{3/2}}{n_i} \text{ (s)},$$

$$\Lambda_{ee} = 16.05 - \frac{\ln(n_e)}{2} + \ln(T_e) \approx 16 \quad (2.2)$$

where the units of T_e and T_i are keV and n_e is 10^{19} m^{-3} , and where τ_{ei} is the electron–ion collision time, τ_{ee} is the electron–electron collision time, m_p is the proton mass, m_e is the electron charge, M is the atomic mass number, Z is the atomic charge number, Λ_{ee} is the electron–electron Coulomb logarithm, and q_e is the electron charge. The approximations are shown to demonstrate the basic parameter dependencies and are not used in the calculations presented in this paper.

To illustrate the ion heating levels and ion power ‘deposition’ profiles that can be achieved, the energy exchange p_{e-i} is calculated from representative synthetic profiles of T_e , T_i and n_e , as shown in figure 2, using truncated Gaussian profile shapes. These profiles are explicitly taken as the inputs to the p_{e-i} calculations only, and do not represent any transport analysis, nor indicate whether they are achievable in W7-X. The ion temperature profile has been kept fixed to represent the ‘clamped’ $T_{i,0} = 1.5$ keV, whereas for the electron profiles, the central $T_{e,0}$ is varied from 2 keV to 6 keV and a representative central density $n_{e,0} = 7 \times 10^{19} \text{ m}^{-3}$ is chosen. On axis, the calculated $p_{e-i,0}$ increases with T_e until it saturates at $T_e \sim 4$ keV, but the exchange power profile shape continues to broaden for the entire T_e range considered; see

figure 2(b). In other words, there is a limit to how much the central ion heating can be enhanced by increasing the temperature difference, due to the $\frac{(T_e - T_i)}{T_e^{3/2}}$ term in p_{e-i} , but the heated volume can be increased. The ion heat flux Q_i is defined by $A \cdot Q_{i(r)} = \int_0^r p_{e-i} \frac{dV}{dr} dr$, where A is the flux surface area at r . As an example, figure 2(c) shows that at the central location $r/a = 0.3$, Q_i saturates for $T_e > 3$ keV, whereas further out at $r/a = 0.6$, it can continue to rise to $T_e = 6$ keV. However, for electron-heated plasmas, the central ion heating can be enhanced by increasing the electron density, as is illustrated in figure 2(d) for fixed values of $T_{e,0} = 3$ keV and $T_{i,0} = 1.5$ keV. Due to the n_e^2 term in p_{e-i} , the on- and off-axis heat flux Q_i increases simultaneously. In experiments, fixing $T_{e,0} = 3$ keV would require that n_e and P_{ECRH} are simultaneously increased.

To conclude, in electron-heated plasmas, the ion heating profile is broad and the heat flux peaks off axis. Whether a broad heating profile can lead to high central temperatures strongly depends on the type of transport at play. In the case of non-stiff diffusive transport this would necessarily lead to broad and flat temperature profiles as were found, for example, for electron heat transport in [24, 31]. However in the case of strong profile stiffness, as is found, for example, in tokamak H-mode plasmas (e.g. [32–34]), the achievable central temperature does not strongly depend on the shape of the heat deposition profile; instead, it is largely determined by the strength of the edge pedestal pressure p_{ped} . The latter lifts up the stiff core profile with $p_{\text{ped}}/p_0 \sim \text{constant}$, and $T_{\text{ped}}/T_0 \sim \text{constant}$.

3. Profile preparation

In order to compare simulated ion and electron temperature profiles with experimental data in W7-X, the measured profiles are required. The electron temperature is measured using Thomson scattering (TS) [35, 36] and validated using electron cyclotron emission (ECE) radiometry [37, 38] diagnostics. The latter depends for its measurement volume localization on calculations using the ray-tracing code Travis [39] and the magnetic field from the equilibrium code VMEC [40]. The line-average plasma density is measured by a single-channel interferometer [41], and the plasma density profile is measured by TS. The ion temperature profile in W7-X is measured by an x-ray imaging crystal spectrometer (XICS) diagnostic [42–44] and a charge exchange recombination spectroscopy (CXRS) diagnostic [45]. To enable CXRS T_i measurements, short 10 ms beam blips (compared to $\tau_E > 100$ ms of neutral beam injection (NBI) heating) are used. The impact on the plasma stored energy is less than $\Delta W_{\text{dia}} = 5\%$

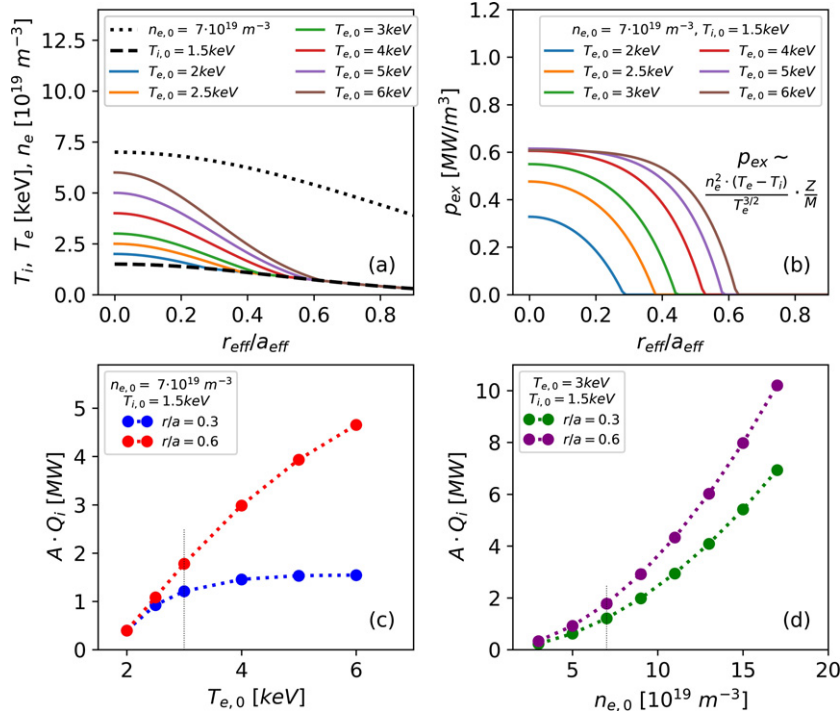


Figure 2. (a) Synthetic profiles of T_e , T_i , and n_e using truncated Gaussians, where $T_e \geq T_i$ is assumed across the profile. $T_{e,0}$ is varied from 2–6 keV and $T_{i,0}$ is set constant at 1.5 keV. The density has a maximum of $7 \times 10^{19} \text{ m}^{-3}$; (b) The electron-to-ion exchange power density p_{e-i} , using the profiles in (a), for a hydrogen gas (charge $Z = 1$ and mass number $M = 1$). (c) The subsequent volume-integrated heat flux $A \cdot Q_i$ in MW up to $r/a = 0.3$ and $r/a = 0.6$, respectively. Also shown in (d) is $A \cdot Q_i$ up to $r/a = 0.3$ and $r/a = 0.6$ for the case where $n_{e,0}$ is varied and both $T_{e,0} = 3 \text{ keV}$ and $T_{i,0} = 1.5 \text{ keV}$ are kept constant. The vertical dashed lines in (c) and (d) are representative of the profiles in figures 15(a) and (b).

(see figure 11). The CXRS ion temperature, the ECE, and the Thomson electron-temperature measurements show excellent consistency in the outer halves of the profiles ($r/a > 0.5$) with good e–i equipartition. The XICS temperature measurement is, however, hampered by as-yet unresolved uncertainties in the instrument profile of the spectrometer. In order to match the T_i values measured by XICS to those measured by CXRS, as well as to the T_e values measured by TS & ECE outside $r/a > 0.5$, the XICS T_i profiles are given a single offset of $\Delta T_i = -100 \text{ eV}$ in all the XICS profiles presented in this paper.

Fits of the experimental profiles are used as inputs for further analysis. The equilibrium for mapping profiles is obtained using the VMEC code [40] with the kinetic profile information as input for an iterative equilibrium calculation. The n_e , T_e , and T_i profiles are fitted using the LOWESS algorithm (locally weighted scatterplot smoothing) (see e.g. [46]) combined with a ‘leave-one-out’ (median) filter to deal with outliers. LOWESS carries out a locally weighted regression of variable y on variable x inside a windowed range and saves the smoothed variable. It is computationally intensive, but offers a stable fit to scattered data. The fit errors are determined by a Monte Carlo error estimation, in which each data point is allowed to move inside its own error margins and the fitting is repeated N times, thus obtaining a set of fits from which the standard deviation σ can be estimated; the 2σ error margins are shown in the profile plots in figures 3, 7 and 15. The LOWESS filter width, the outlier window used for data-point weighting,

was set to $r/a = 0.1$ for the Thomson T_e and CXRS T_i profiles. For the TS density profiles a broader filter width of $r/a = 0.2$ was used due to larger statistical and systematic errors. As the XICS T_i profiles are the result of an Abel inversion [42, 44] no further fitting of this data was applied, but the plotted error margins are a result of the statistical spread of the profiles inside the averaging time window.

Residual profile inconsistencies are observed in the outer regions of the profiles, where $T_e = T_i$ is expected. In order to obtain a meaningful PB we therefore set $T_e = T_i$ in the outer region of the profile beyond the point where T_e and T_i first cross. As good T_i profile quality can only be guaranteed for $r/a < 0.8$, the PB analysis in this paper is restricted to the range within $r/a = 0.6$. Note that as ion heat transport is studied here, the electron temperature is deliberately set equal to the ion temperature, rather than vice versa. In [27], where the electron transport was studied, the reverse was done by setting $T_i = T_e$ from the point where $T_i > T_e$ in the outer region of the plasma.

4. Neoclassical transport compared to experimental findings

In tokamaks, neoclassical transport has an inverse temperature dependence based on proportionality for banana-orbit-like transport. Using $\chi_{\text{NC,tok}} \sim \rho_{\text{pol}}^2/\tau_i$, where τ_i is the ion collision frequency, one can derive $\chi_{\text{NC,tok}} \sim n/\sqrt{T}$ or $\chi_{\text{NC,tok}} \sim T^{-3/2}$ if constant pressure is assumed. On the contrary, neoclassical

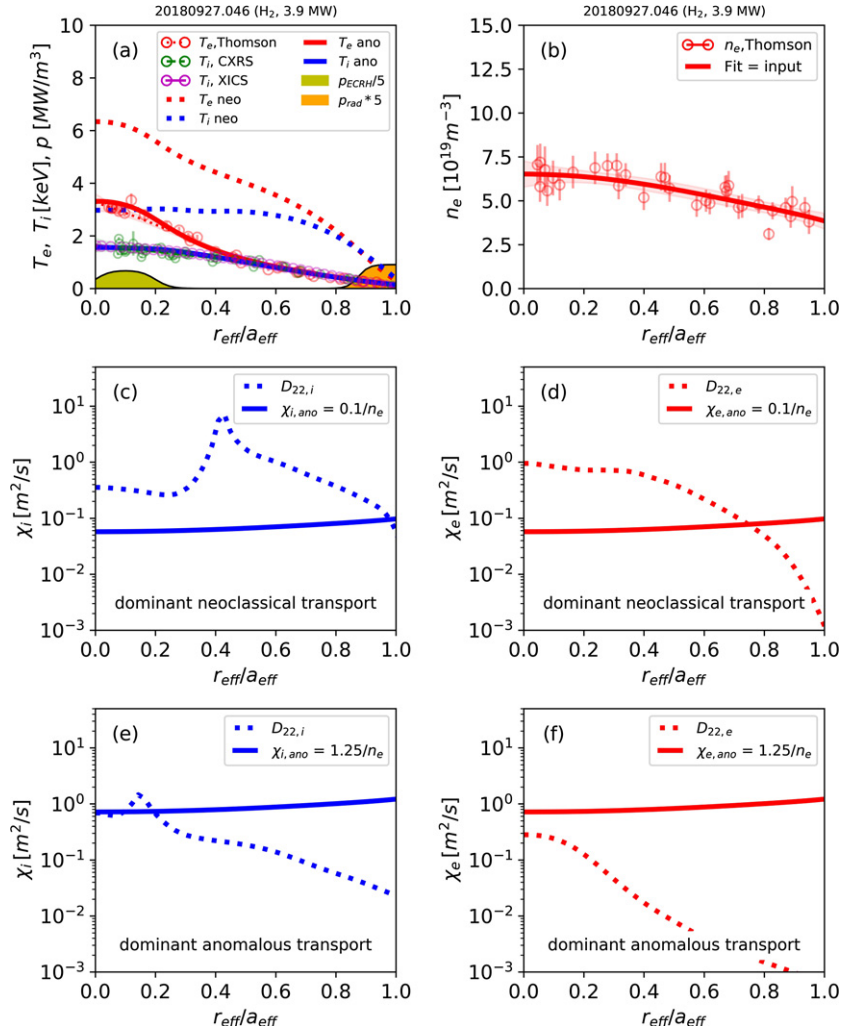


Figure 3. Experimental and modelled profiles of an ECRH plasma with $P_{\text{ECRH}} = 3.9$ MW (20180927.042 $t = 1.1$ – 2.5 s). (a) T_e from TS, and T_i from XICS and CXRS, with modelled profiles using the NTSS and DKES codes in red (T_e) and blue (T_i), and shown by dashed lines for dominant neoclassical (neo) and solid lines for dominant anomalous transport (ano). Also shown are the ECRH deposition and radiated power profiles assumed in both models. (b) The input n_e profile. The ion and electron heat diffusivities used are shown in ((c) and (d)) for the neoclassical dominant model (neo) and in ((e) and (f)) for the dominant anomalous transport model (ano).

stellarator diffusivity has a positive temperature dependence and scales strongly, according to $T^{7/2}$, and somewhat weaker, according to $T^{5/4}$, for the $1/\nu$ (1.1) and $\sqrt{\nu}$ (1.2) collisionality regimes, respectively [4]. Nevertheless, for the optimized W7-X configuration, the low ion-power density in electron-heated plasmas combined with pure neoclassical transport does not lead to ion temperature clamping at $T_i \sim 1.5$ keV as observed in experiments. Indeed, figure 1 shows that the neoclassical transport with the lowest effective magnetic ripple $\langle \varepsilon_{\text{eff}} \rangle = 0.8\%$ in W7-X should produce $T_i > 3$ keV for densities roughly greater than $7 \times 10^{19} \text{m}^{-3}$. The ion temperature would then indeed saturate, but at roughly double the ion temperature than that observed experimentally.

Figure 3 shows an example of the experimental profiles of a hydrogen-fueled ECRH plasma with $n_{e,0} = 7 \times 10^{19} \text{m}^{-3}$ with $P_{\text{ECRH}} = 3.9$ MW, a total radiative power $P_{\text{rad}} = 1.8$ MW, and $T_{e,0} = 3.3$ keV, $T_{i,0} \sim 1.6$ keV in the standard configuration with $\langle \varepsilon_{\text{eff}} \rangle = 0.8\%$ and $Z_{\text{eff}} = 1.3$. The ECRH heat deposition profile is calculated from the launch geometry using VMEC

for equilibrium and the TRAVIS code for ray tracing [39]. The radiation loss profile is estimated from bolometer inversion profiles and is located towards the edge of the plasma [47, 48], as can be seen in appendix A. The stored energy and normalized pressure of this plasma are $W_{\text{th}} = 0.5$ MJ with a normalized pressure of $\langle \beta \rangle \sim 0.5\%$, and $\tau_{\text{E,exp}}/\tau_{\text{ISS04}} = 0.65$.

Also shown are simulated profiles using the NTSS transport code [28] with the central ECRH deposition profile and a fixed density profile (fit) taken from figure 3(b). The neoclassical mono-energetic transport coefficients are calculated using the DKES code [29]. In the first run only a small amount of anomalous transport is assumed as $\chi_{\text{ano}} = 0.1/n_e < 0.1 \text{m}^2 \text{s}^{-1}$ across the profile for both ions and electrons, to avoid using unrealistically small neoclassical diffusivity D_{22} at the plasma edge, following a similar approach to that described in [29]. Figures 3(c) and (d) show that in this predictive run, the transport is dominated by electron and ion neoclassical heat transport for the core plasma $r/a < 0.75$. As a result, the NTSS code in this case not only predicts a much higher central $T_{i,0}$ (and

$T_{e,0}$) than those of the experiment, but the T_i and T_e profiles are also much broader than observed experimentally. This simulated plasma therefore has a much higher global performance with $W_{\text{th,NC}} = 1.6$ MJ, $\langle\beta_{\text{NC}}\rangle \sim 1.5\%$, and $\tau_{\text{E,NC}}/\tau_{\text{ISS04}} = 2.1$. This agrees with the findings of [29], in which similarly low but not identical levels of turbulent transport were assumed.

For the NTSS simulations to match the experimental global performance and profiles, the anomalous heat diffusivity must be increased by an order of magnitude to $\chi_{\text{ano}} = 1.25/n_e \sim 0.7\text{--}1$ m² s⁻¹. In this case, the neoclassical transport is overshadowed by the anomalous transport, as can be seen in figures 3(e) and (f). Similarly to the situation in the experiment, the plasma performance suffers strongly from anomalous transport, and in these simulations $W_{\text{th,anom}} = 0.5$ MJ, the normalized pressure $\langle\beta_{\text{anom}}\rangle \sim 0.5\%$, and $\tau_{\text{E,anom}}/\tau_{\text{ISS04}} = 0.65$, replicating the performance found in the experiment. Even though we have applied an ad hoc model for the turbulent transport, the high level of anomalous transport that is required to match the experimental findings clearly implies that the heat transport in the ECRH plasma in figures 3(a) and (b) is likely dominated by turbulent rather than neoclassical transport.

Electron turbulent transport was experimentally studied in [27]. In an electron heat transport study using ECRH modulations at density of $n_{e,0} \sim 4 \times 10^{19}$ m⁻³, the PB and HPP transport could be separately identified. The analysis in a *standard configuration* plasma found that the average PB diffusivity in the core plasma was $\langle\chi_{\text{PB,e}}\rangle \approx 0.6 \pm 0.2$ m² s⁻¹. Furthermore, the electron turbulent heat transport appeared largely diffusive, (1) as no clear critical normalised electron temperature gradient ($a \cdot \frac{\nabla T_e}{T_e}\bigg|_{\text{crit}} = a/L_{T_e,\text{crit}}$) was found, which meant that it was hard to distinguish between ETG or TEM types of turbulence as the driving transport mechanism; (2) HPP experiments using wide parameter variations showed that the electron turbulent transport features only a low degree of transport stiffness with $\chi_{\text{HP,e}}/\chi_{\text{PB,e}} < 2$. Moreover, the electron heat transport shows only a small configuration dependence and no strong density dependence, and only a weak positive power dependence was found. The study of the ion turbulent heat transport is the topic of the paper at hand.

5. Modelling of ion turbulent heat transport

The anomalous *ion*-heat-transport in fusion experiments is generally determined by ITG turbulence, which means there is a limit on the inversed gradient length a/L_{T_i} . In tokamaks, this causes a high degree of ion profile stiffness [49–54], such that their energy confinement is largely controlled by the achievable edge (ion) temperature, or the so-called pedestal temperature. In [55] the destabilization of the ITG modes in stellarators is compared to that in tokamaks by means of linear gyro-kinetic calculations using the GENE code [23]. The authors of that paper discovered remarkably similar results for both confinement concepts. Important factors for the ITG growth rate are the ratio T_e/T_i and the normalized density gradient ($a \cdot \frac{\nabla n}{n} = a/L_n$). The temperature ratio T_e/T_i has a strong destabilizing effect on the ITG modes, whereas a/L_n has a stabilizing effect in the absence of trapped electrons. The latter is of utmost important when considering avenues

that can suppress ITG turbulence, as is done in e.g. post-pellet experiments [7, 8, 56]. In W7-X, with its beneficial 3D properties [5, 6], a so-called stability valley with elevated $a/L_{T_i} = a/L_n$ can be achieved when ITGs and density-gradient-driven TEMs, or so-called iTEMs, are simultaneously suppressed [6, 7]. For a comparison between the ECRH plasma experiments and the low-density gradients described in this paper, gyro-kinetic calculations were applied with kinetic electrons as well as kinetic ions. Both linear as well as nonlinear gyro-kinetic calculations were conducted. As non-linear gyro-kinetic calculations are very expensive in terms of computer time, a smaller subset of simulations was conducted. Both the linear and nonlinear runs were performed for the most unstable flux tube, where the most unstable flux tube was selected from several runs at different poloidal angles. Note that the simulations presented here act as a qualitative comparison to the experimental data and that a quantitative comparison has currently not been conducted.

In the linear simulations, the flux-tube average calculations are conducted with the normalized density gradient fixed at $a/L_n = 0.5$ and the normalized electron temperature gradient at $a/L_{T_e} = 0$. Although in experiments $a/L_{T_e} \geq a/L_{T_i}$, the assumption $a/L_{T_e} = 0$ is representative, as the impact of a/L_{T_e} on ITG turbulence is small. Figure 4(a) shows the linear growth rate of such calculations using the W7-X ‘standard’ equilibrium for a wide range of temperature ratios $T_e/T_i = 1\text{--}5.5$. Quite clearly, the ratio T_e/T_i enhances the degree of transport stiffness, i.e. the slopes of the curves in figure 4(a). Hence, electron heating can indirectly intensify ion transport as T_e/T_i is increased.

Nonlinear flux surface gyro-kinetic simulations can calculate the normalized heat flux Q_i/Q_{GB} required to sustain a given a/L_{T_i} . The gyro-Bohm diffusivity χ_{GB} and hence the gyro-Bohm heat flux Q_{GB} are defined, for example in [57]:

$$\chi_{\text{GB}} = \frac{\rho_i^2 c_i}{a} = \sqrt{\frac{m_i}{e}} \frac{T_i^{3/2}}{aB^2} \quad (3.1)$$

$$Q_{\text{GB}} = \frac{\rho_i^2 c_i P_i}{a^2} = \sqrt{\frac{m_i}{e}} \frac{n_i T_i^{5/2}}{a^2 B^2}, \quad (3.2)$$

where $\rho_i = \sqrt{m_i T_i / eB}$ is the ion Larmor radius, $c_i = \sqrt{eT_i / m_i}$ is the ion sound speed using the ion temperature in eV, m_i is the ion mass in kg, P_i is the ion pressure, and a is the effective minor radius. The nonlinear calculations are conducted with a normalized density gradient $a/L_n = 0$ and a normalized electron temperature gradient $a/L_{T_e} = 0$. Qualitatively, the nonlinear calculations are consistent with the linear calculations, although the critical gradient ($a/L_{T_i}\big|_{\text{crit}}$ (zero crossing of the simulations through the ordinate), appears to be increased with respect to the linear calculations. This nonlinear upshift of $(a/L_{T_i}\big|_{\text{crit}})$ compared to linear gyro-kinetic simulations was first reported in [58] and is also known as the Dimits shift.

The important result is that both linear as well as nonlinear calculations show that the ratio T_e/T_i exacerbates the ITG-induced transport and increases the degree of ion temperature profile stiffness. In predominantly electron-heated plasmas, usually with $T_e/T_i \geq 1$, plasma heating can strongly enhance

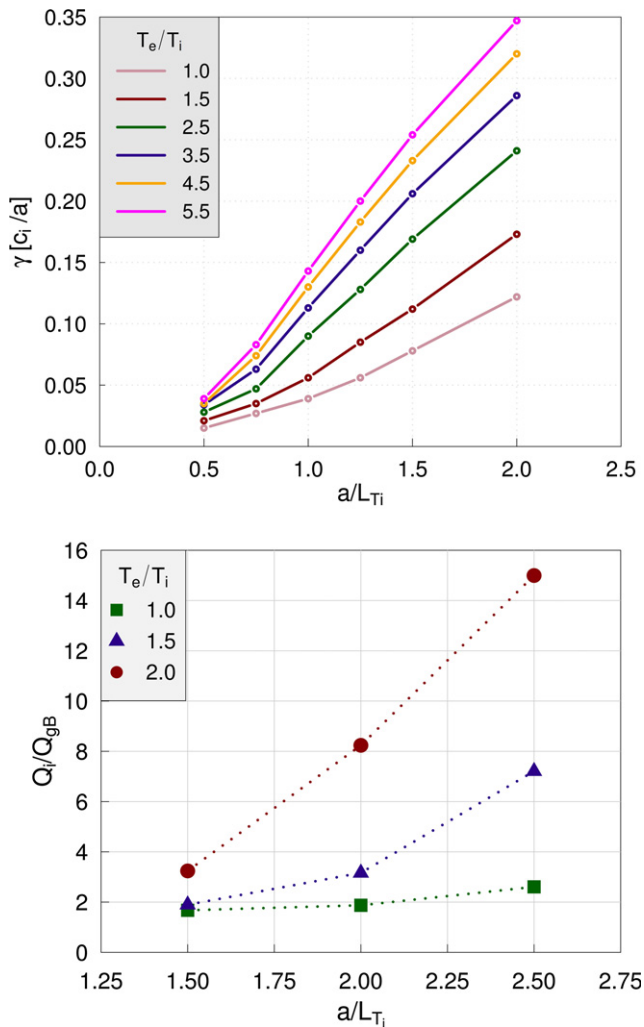


Figure 4. Gyro-kinetic simulations showing the enhancement of profiles stiffness in ITG turbulent transport as the ratio T_e/T_i is increased (top): linear flux tube averaged gyro-kinetic simulations, showing the growth rate γ of the most dominant ITG mode as a function of the normalized ion temperature gradient a/L_{T_i} ; (bottom): nonlinear flux surface averaged simulations showing the normalized ion heat flux Q_i/Q_{GB} in gyro-Bohm units as a function of a/L_{T_i} . The gyro-Bohm heat flux Q_{GB} is given by expression (3.2) in the main text. Both simulations use kinetic electrons and kinetic ions. As the nonlinear simulations are costly in terms of the required calculation time, fewer steps in a/L_{T_i} and fewer values of T_e/T_i have been used.

ion turbulent transport and help in saturating or clamping the achievable ion temperature.

As already reported in [57], the choice of magnetic configuration may affect the ITG stability. However, for the four configurations shown in figure 1, ion temperature clamping occurs at the same level of $T_i \sim 1.5 \pm 0.2$ keV. In the context of ITG turbulent transport this may imply that either (1) the turbulence response is very similar between these configurations, e.g. [6], or (2) the initial underlying profile stiffness differences may be obscured by the strong T_e/T_i effect described above. Therefore, characterizing the perturbative ion transport in W7-X configurations requires a different tool than the simple PB analysis presented in this paper. For example, ion-heat-pulse-propagation studies require a hardware upgrade

to faster spectrometers and the data acquisition of our CXRS diagnostic. Using e.g. NBI modulation experiments, one could then follow an equivalent strategy to that described for electron perturbative transport in [27]. This spectrometer upgrade is planned to be implemented and will hopefully be available in the next experimental campaign.

In the remainder of this paper we will select only the standard configuration with the best NC transport reduction to study the turbulent ion transport in detail. We first investigate how well the ion temperature clamping as seen in W7-X electron-heated plasmas can be explained by assuming gyro-Bohm-level turbulent transport without the additional ITG features described by the theory above. A dedicated set of experiments will then be selected with a variation of the ion heat flux that is as wide as possible, to see whether, from a simple PB argument, evidence for ITG signatures such as profile stiffness or turbulence-enhancing T_e/T_i can be observed.

For the gyro-Bohm modelling we use the NTSS code and the density profile shape from the fit in figure 3(b), as well as a representative level of 50% plasma radiation in the outer plasma volume $r/a < 0.8-1$. As a boundary condition for the separatrix, $T_i = T_e = 100$ eV is assumed. For the electron transport we assume a power independent diffusivity $\chi_{e,turb} = 0.7 \text{ m}^2 \text{ s}^{-1}$, which represents the upper limit of the anomalous diffusivity found in [27]. For the ions we assume a gyro-Bohm diffusivity $\chi_{i,turb} = \chi_{GB}$ that follows equation (3.1).

In the simulations we vary the central electron density from $2-9 \times 10^{19} \text{ m}^{-3}$ and apply electron heating using the typical ECRH deposition profile for X2 heating from figure 3(a). For each density and power level we allow NTSS to calculate the T_e and T_i profiles using the neoclassical and anomalous transport coefficients described above, where $\chi_{i,turb} = \chi_{GB}$ is allowed to vary dynamically with T_i across the plasma cross section. The simulation results are shown in figure 5. Interestingly, some of the features found in the experiment are seen in this simple simulation exercise. The central ion temperature indeed saturates at a level close to $T_{i,0} \sim 1.5$ keV. Moreover, there appears to be only a small density dependence on the T_i saturation, certainly when we take a power-dependent radiative density limit into account following [14]. The difference in the power dependence on the saturation level seen in figure 5(a) may be due to the fact that a fixed $\chi_{e,turb} = 0.7 \text{ m}^2 \text{ s}^{-1}$ is chosen, whereas [27] reports a weak power dependence of $\chi_{e,turb}$. The normalized pressure $\langle \beta \rangle = \langle p \rangle / (B^2 / 2\mu_0)$, where $\langle p \rangle$ is the volume-averaged plasma pressure, is somewhat higher than that found in the experiment, where typically $\langle \beta \rangle \sim 0.5\%$ for the highest density and input power used in the simulations.

A realistic upper limit for the installed ECRH power in W7-X is 15 MW. In [29], a projection was conducted that assumed mostly neoclassical transport and a turbulence model for the edge plasma. Keeping the overpredictions of the neoclassical transport simulation in figure 3 in mind, we would like to see what the gyro-Bohm model would predict for the higher ECRH levels for a comparison with the results in [29], and to get insight in future performance. Using the same model as that used in figure 5, and following the same approach as in [29], figure 6 ‘predicts’ the performance with upgraded ECRH

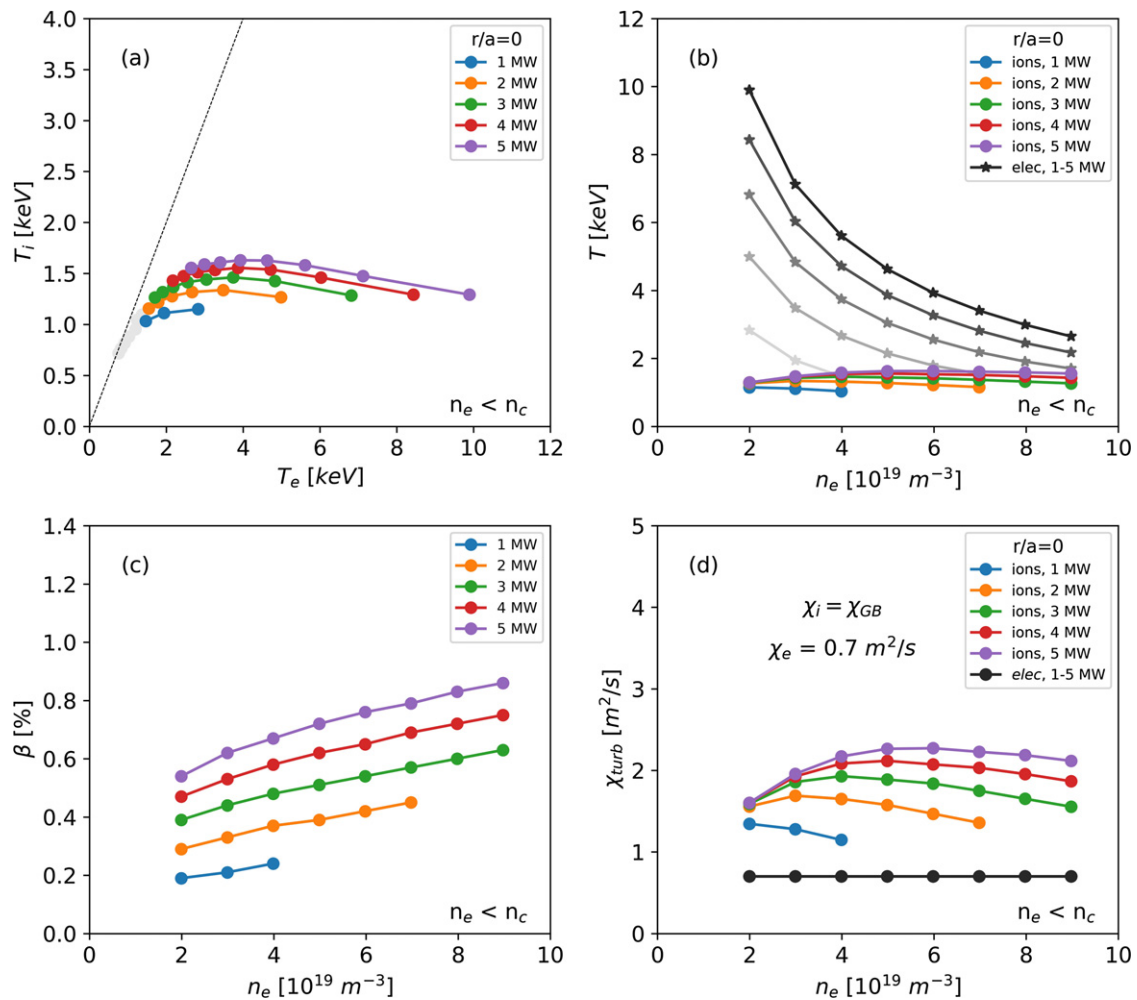


Figure 5. Transport simulation using the NTSS code with varying values of $n_{e,0}$ and P_{ECRH} , applying a gyro-Bohm transport $\chi_{i,\text{turb}} = \chi_{\text{GB}}$ for the ions, and an electron heat diffusivity of $\chi_{e,\text{turb}} = 0.7 \text{ m}^2 \text{ s}^{-1}$ as a typical value for the diffusive electron heat transport. The shape of the electron density profile is taken from the experiment as an input. (a) shows the achieved central T_i and T_e versus the central electron density n_e . (c) features the normalized volume-averaged pressure $\langle\beta\rangle$ as a function of n_e and (d) shows the assumed turbulent heat diffusivities, where $\chi_{i,\text{turb}} = \chi_{\text{GB}}$ varies according to $T_i^{3/2}$. The critical density $n_c = 0.5^* P^{0.6}$ is the density above which a radiative collapse will occur for a given input power P and is derived from [14]. The simulation points where $n_e > n_c$ are not included.

power, in terms of confinement normalized to the ISS04 scaling $\tau_E/\tau_{\text{ISS04}}$ as well as the achievable normalized pressure $\langle\beta\rangle$. The density profiles are scaled up to the experimental limit of the ECRH-O2 heating scheme, which is $n_{e,0} = 1.6 \times 10^{20} \text{ m}^{-3}$. This ion gyro-Bohm transport model extrapolates the central ion temperature to be $T_{i,0} \sim 2 \text{ keV}$ at $P_{\text{ECRH}} = 15 \text{ MW}$, and when T_e approaches T_i at the higher density, the confinement and normalized pressure fall well below the projections of [29]. The model produces a slightly more beneficial power scaling and a weaker density scaling than the ISS04 scaling, and the results may therefore even be ‘optimistic’.

Naturally, the model is for demonstration purposes, and for this reason no sensitivity analysis is provided. We will next study ion heat transport by means of a power balance study of ECRH-heated plasmas. Using a well-selected set of experiments, we study the local heat transport and investigate whether any of the ITG features, such as the T_e/T_i effect, can be seen in the experiment.

6. Ion transport in an ECRH power scan

To allow a probe of the ion heat transport, a detailed PB comparison is conducted of both a hydrogen and a helium fueled plasma in appendix A with ECRH power steps ranging from 3.9 to as low as 1.2 MW. Due to the higher critical radiative density limit of helium, compared to that of hydrogen plasmas, a broader power scan is possible in helium. For this reason, helium plasmas are better suited to probing the ion transport, as a wider variation of the exchange power is possible at a constant high density. The high density of $\langle n_e \rangle = 7 \times 10^{19} \text{ m}^{-3}$ is required to ensure that ion root transport is guaranteed for all power steps. At lower plasma densities, electron-to-ion root transitions occur at varying positions in the profile, depending on the power level (see e.g. [22]). Such transitions complicate the study of the anomalous heat flux $Q_{\text{turb}} = Q_{\text{exp}} - Q_{\text{NC}}$. Furthermore, the transport gap, or the ratio $Q_{\text{turb}}/(Q_{\text{exp}} - Q_{\text{NC}})$, grows in W7-X ECRH plasmas as the density increases,

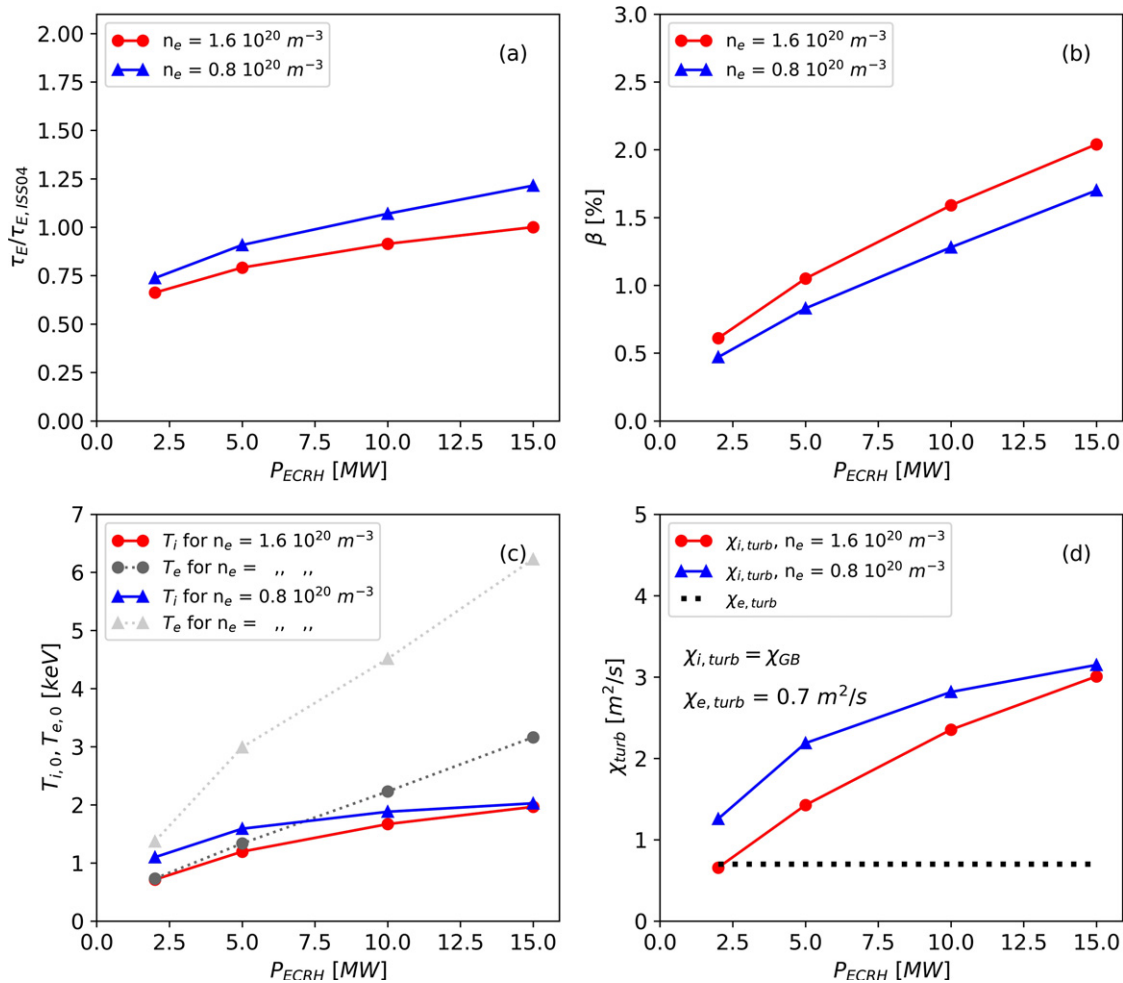


Figure 6. Extrapolation of the plasma performance with up to $P_{\text{ECRH}} = 15$ MW of centrally deposited heating power using an ion gyro-Bohm transport model. (a) energy confinement scaling of $\tau_E/\tau_{\text{ISS04}}$; (b) volume-averaged pressure; (c) ion and electron central temperatures and (d) the central ion and electron turbulent heat diffusivities used in the model predictions.

further improving the accuracy in determining Q_{turb} . Finally, in appendix A, it is shown that the transport properties of the H- and He-fueled plasmas are virtually the same. Therefore, the larger power scan in the helium-fueled plasma is used to probe the ion transport in these electron-heated plasmas. The helium fuel purity is 70% He and 30% H, but this is high enough to have a beneficial effect on elevating the critical density.

The power scan from 3.9 MW down to 1.2 MW in the helium plasma shows that with decreasing P_{ECRH} , the central electron temperature decreases from 3 keV to 1.3 keV (figure 7(a)). The ion temperature variation is smaller and $T_{i,0}$ reduces from 1.7 keV to 1.2 keV. The density profile remains virtually unchanged for the entire power scan (figure 7(b)). The T_e , T_i , and n_e profile fits and their error bars (shaded area in figures 7(a) and (b)) are used to calculate the subsequent parameters and their error bars¹ in figure 7(c) onwards

¹ The error ranges of the derived parameters are obtained by propagating the T_e , T_i , and n_e errors in the NTSS code using three data inputs: (1) the fits as T_e , T_i , and n_e , (2) the fits as $[T_e + dT_e]$, $[T_i + dT_i]$, and $[n_e - dn_e]$ and (3) $[T_e - dT_e]$, $[T_i - dT_i]$, and $[n_e + dn_e]$.

and the rest of this document. The ambipolar radial electric field, as calculated by NTSS, remains in the ion root during the scan (figure 7(c)), as confirmed by CXRS and Doppler reflectometry (DR) measurements of E_r . The calculated neo-classical heat fluxes Q_{NC} , $Q_{i,\text{NC}}$, and $Q_{e,\text{NC}}$ stay much lower than the total experimental heat fluxes Q_{exp} , $Q_{i,\text{exp}}$, and $Q_{e,\text{exp}}$, (figures 7(d)–(f)), and thus turbulent transport stays dominant when P_{ECRH} is varied in the scan. The turbulent ion heat flux $Q_{i,\text{turb}} = Q_{i,\text{exp}} - Q_{i,\text{NC}}$ varies from 0.8 MW down to 0.1 MW from the highest to the lowest ECRH power level (normalized to n_i values in figure 7(g)). The response of the ion temperature to the decreasing ion heat flux appears curious at first: figure 7(j) shows how the T_i profile changes shape during the power scan: outside $r/a \sim 0.5$, the normalized ion temperature gradient a/L_{T_i} increases, whereas inside this radius it decreases with increasing ion heat flux $Q_{i,\text{turb}}$. The turbulent ion heat diffusivity $\chi_{i,\text{turb}}$ (figure 7(i)) is calculated using $Q_{i,\text{turb}} = n_i \cdot \chi_{i,\text{turb}} \cdot \nabla T_i$. In the ECRH downward power scan, this heat diffusivity reduces from $1 \text{ m}^2 \text{ s}^{-1}$ down to $0.1 \text{ m}^2 \text{ s}^{-1}$ averaged over $0.2 < r/a < 0.8$. As expected from the variation of the T_i profile shapes, it is found that at a small radius of $r/a = 0.3$,

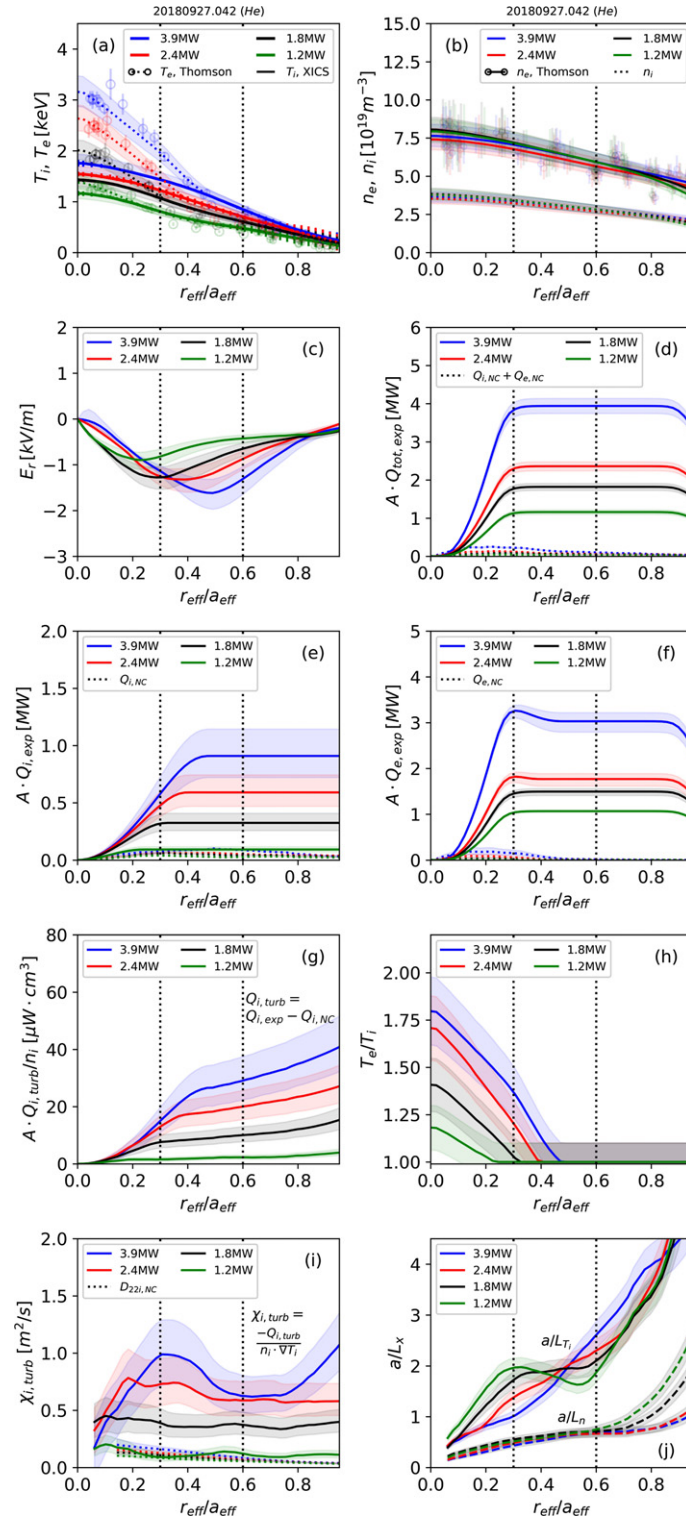


Figure 7. Profile comparison of an ECRH power scan in He-fueled plasma from PECHR = 3.9 to 1.2 MW. (a) T_i as measured by x-ray imaging spectroscopy (XICS) and T_e measured using TS. (b) n_e measured using TS and n_i derived therefrom using $Z_{\text{eff}} \sim 2$ from bremsstrahlung, (c) ambipolar radial electric field E_r . (d) Total experimental volume integrated heat flux $A \cdot Q_{\text{tot,exp}}$ (solid) compared to the total neoclassical integrated heat flux $A \cdot Q_{\text{tot,NC}}$ (dashed); A is the flux surface area. (e) Experimental integrated ion heat flux $A \cdot Q_{i,\text{exp}}$ (solid) as calculated from the exchange power, compared to the neoclassical integrated ion heat flux $A \cdot Q_{i,\text{NC}}$ (dashed). (f) Experimental integrated electron heat flux $A \cdot Q_{e,\text{exp}}$ (solid) compared to the neoclassical integrated electron heat flux $A \cdot Q_{e,\text{NC}}$ (dashed). (g) Turbulent ion heat flux normalized to the ion density $A \cdot Q_{i,\text{turb}}/n_i$. (h) Profiles of T_e/T_i (i) turbulence ion heat diffusivity (j) normalized ion temperature gradient a/L_{T_i} compared to the density gradient length a/L_n , where $L_x = x/\nabla x$. The vertical drawn lines indicate the radii of the analyses in figures 8 and 9.

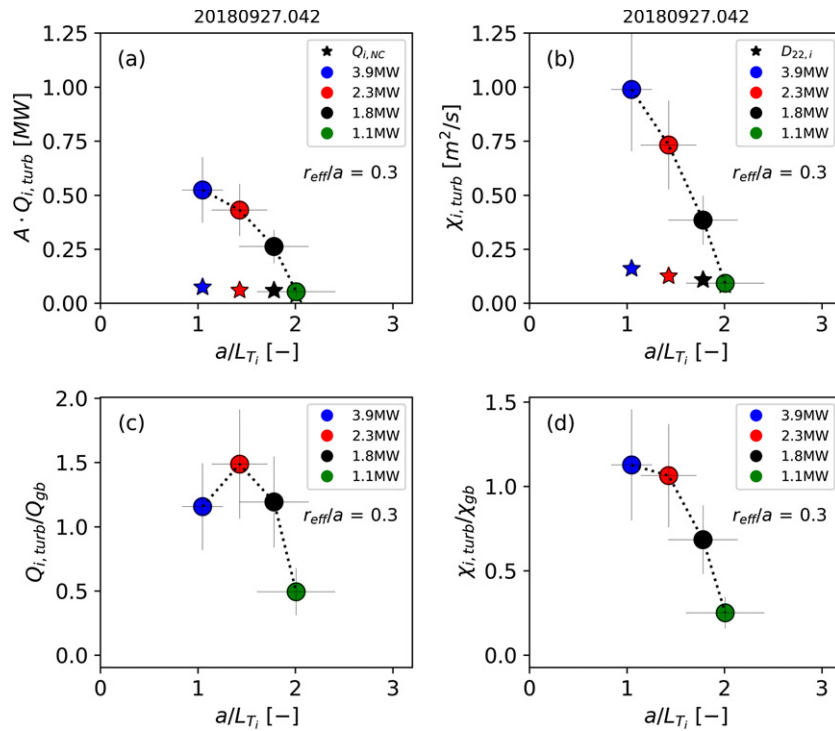


Figure 8. For radius $r_{eff}/a_{min} = 0.3$: response of normalized ion temperature gradient a/L_{T_i} to (a) turbulent ion heat flux $Q_{i,turb}$ times the flux surface area A , in MW, (b) turbulent ion heat diffusivity $\chi_{i,turb}$ in $m^2 s^{-1}$ as well as (c) turbulent ion heat flux $Q_{i,turb}$ in gyro-Bohm units (equation (3.1)) and (d) turbulent ion heat diffusivity $\chi_{i,turb}$ in gyro-Bohm units (equation (3.2)).

the inversed gradient length a/L_{T_i} shrinks with increasing heat diffusivity $\cdot \chi_{i,turb}$ and at a larger radius of $r/a = 0.6$, it increases with increasing heat diffusivity.

The inverse responses of a/L_{T_i} at $r/a = 0.3$ and $r/a = 0.6$ respectively, to an increase in (a) the turbulent heat flux and (b) the diffusivity are summarized in figures 8 and 9, where in (c) and (d), the turbulent heat flux and heat diffusivity are also shown normalized to the gyro-Bohm heat flux and diffusivity as given by equations (3.1) and (3.2), respectively. The strong T_i dependence of the gyro-Bohm normalization compresses the range covered, and for the highest ECRH power actually leads to a reduction of the normalized heat flux compared to the second-highest ECRH power in figure 8(c). Nevertheless, at this small radius, it appears, rather counterintuitively, that the reduction in the normalized gradient length a/L_{T_i} is due to an apparent ‘negative’ ion temperature profile stiffness. Clearly, a strong transport driver is at play that reduces the local gradient $\nabla T_i/T_i$ despite an increase in the heat flux. This observation is in qualitative agreement with the theoretical simulations, in which the ratio T_e/T_i enhances ITG turbulence, and at a stagnating heat flux Q_i/Q_{GB} can even lead to a reduction of a/L_{T_i} . Indeed, in the experiment the ratio T_e/T_i increases from 1 to 1.5 with increasing P_{ECRH} at $r/a = 0.3$. Further out, at $r/a = 0.6$, the ratio $T_e/T_i \sim 1$ for all four power steps, and the ITG simulations in figure 4 show that at low T_e/T_i , it is easier to drive a local ion temperature gradient with a modest increase of (normalized) heat flux.

The gyro-kinetic simulation examples in figure 4 indicate that the increase of the ion transport stiffness due to the temperature ratio can be strong indeed and may impose a

limit on T_i . This additional driver for turbulence is inherent to electron-heated plasmas: an increase of the ECRH power enhances T_e , which simultaneously enhances the exchange power p_{e-i} as well as exacerbating the ITG turbulence and the degree of T_i profile stiffness. These combined mechanisms cause additional clamping of $\nabla T_i/T_i$, and their integrated effect can contribute to the clamping of the central T_i value, as seen in the entire W7-X database of ECRH-heated plasmas in figure 1. A direct comparison of the experimental observations with the gyro-kinetic simulations is computationally expensive and will be the subject of future theoretical and experimental comparisons.

7. Conclusions and discussion

Ion temperature clamping in ECRH heated plasmas in W7-X is likely a result of various factors that lead to a reduction in the local ion temperature gradients and the global plasma performance. First, the ion heating through exchange power in electron-heated plasmas features a broad heating pattern with a subsequently low power density (figure 2), which under neoclassical transport conditions already produces low ion temperature profile peaking (figure 3). Furthermore, the neoclassical transport is only a fraction of the total transport and in some cases represents as little as 10% of the total transport. As a result, the experimentally achieved T_i -profiles are well below the neoclassical predictions (see e.g. figure 3). The impact of the ion turbulent transport is reasonably well modeled, assuming ion-gyro-Bohm heat transport. The saturation of the central ion temperature with increasing heating power and increasing

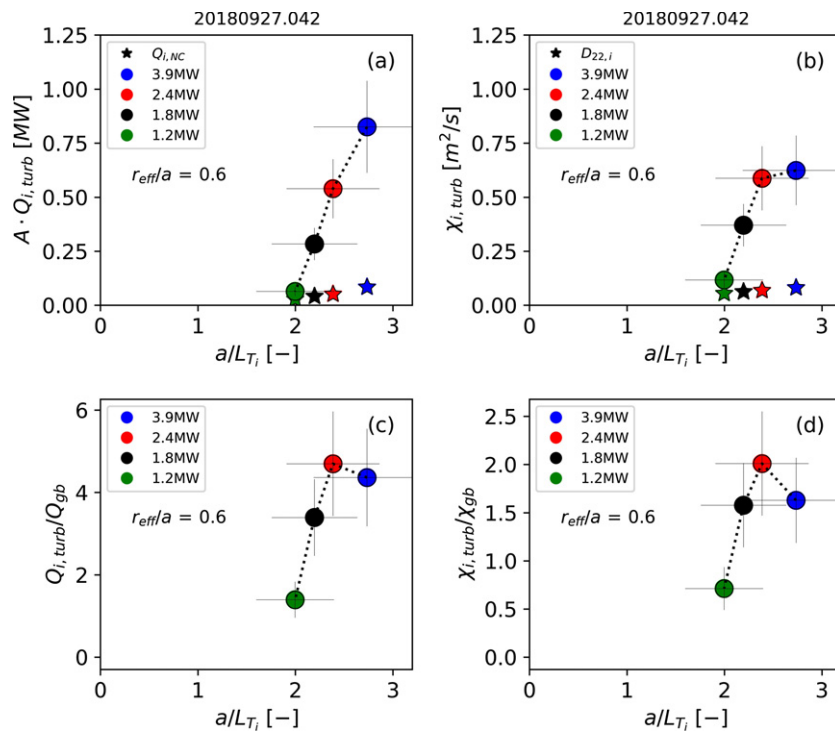


Figure 9. For radius $r_{\text{eff}}/a_{\text{min}} = 0.6$: response of normalized ion temperature gradient a/L_{T_i} to (a) turbulent ion heat flux $Q_{i,\text{turb}}$ times the flux surface area A , in MW, (b) turbulent ion heat diffusivity $\chi_{i,\text{turb}}$ in $\text{m}^2 \text{s}^{-1}$ as well as (c) turbulent ion heat flux $Q_{i,\text{turb}}$ in gyro-Bohm units (equation (3.1)) and (d) turbulent ion heat diffusivity $\chi_{i,\text{turb}}$ in gyro-Bohm units (equation (3.2)).

density is well captured; however, obtaining the details of the ion temperature gradient response to increasing ion heat flux will require further characteristics of ITG turbulence.

A key result from linear and non-linear GENE simulations for the W7-X standard configuration is that the degree of profile stiffness increases with an increase in the ratio T_e/T_i , or, in other words, ITG turbulent transport is exacerbated by T_e/T_i . In the power scan experiment discussed in this paper, indeed it seems that the ‘‘apparent negative profile stiffness’’ as seen at the radius of $r/a = 0.3$, see figure 8, may be caused by the enhancement of turbulence by the T_e/T_i effect as well by the saturation of Q_i/Q_{gb} . At larger radii, where $T_e = T_i$ across the power scan, this effect is mitigated (figure 9).

The enhancement of ITG turbulence with the T_e/T_i ratio is present in both tokamaks and stellarators [55] and appears to be present in all the magnetic configurations shown in figure 1. However, it appears that in tokamaks, linear gyro-kinetic simulations which focus on the strongest growing mode can quantitatively describe the degree of ion transport stiffness enhancement due to T_e/T_i . Therefore, these linear calculations can be used in transport-predictive codes such as ‘trapped gyro-Landau-fluid’ (TGLF) [59]. However, for stellarators, due to their 3D geometry, the non-linear calculations show that the transport enhancement due to T_e/T_i is enhanced by initially less dominant modes; the T_e/T_i parameter affects all possible eigenmodes, including the subdominant ones, which are formally absent from the initial value solution of the linear gyro-kinetic equation in figure 4. In turbulence simulations, however, these subdominant modes also contribute to

the determination of the ion heat flux level. It is therefore expected that the collective effect of the T_e/T_i parameter will be enhanced, as manifested in the nonlinear simulations.

As a result, a predictive transport model that could explain the clamping of the T_i gradients would need to be based on nonlinear gyro-kinetic calculations, which are very costly, and a program such as TGLF will not be readily implementable for W7-X. Therefore, ad hoc transport models that use the outcome of nonlinear calculations and the stiffness enhancement due to an increase in T_e/T_i and its subsequent effect on temperature clamping could be useful tools going forward. In [60], for example, this was done by including the beneficial effect of introducing a density gradient on suppressing turbulence. This tool could be extended with the newly found detrimental effect of T_e/T_i on turbulence.

However, T_i clamping can be broken, as has been shown experimentally. Figure 10 shows a few examples in which the clamping has been broken. The physics mechanism that acts on the turbulence suppression is thought to be the same in these examples; the introduction of a strong(er) density gradient, which aids the reduction or suppression of ITG turbulence and simultaneously limits the density-gradient-driven TEM turbulence. For reference, the figure also shows the power steps in helium- and hydrogen-fueled plasmas with the labels (1) and (2), as discussed in this paper. Both show that with everything else held constant, T_i rises slowly from low to high ECRH power and the maximum T_i value achieved, $T_i \sim 1.6$ keV, is similar between the two plasmas. Also, as a comparison with label (2a), a power-step experiment at half the density of used

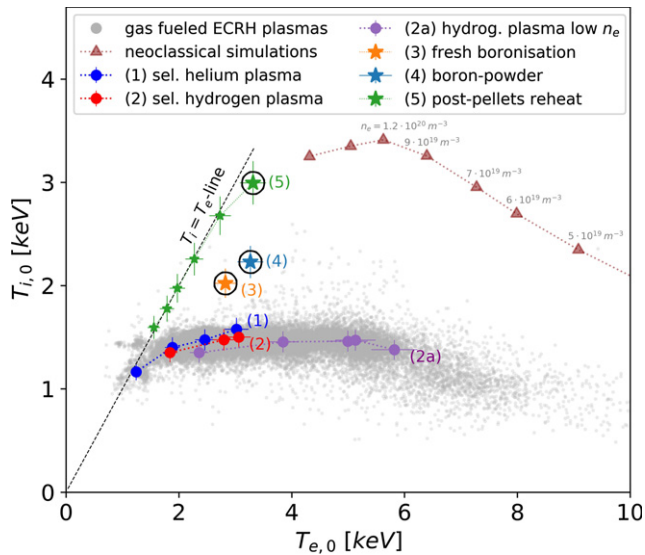


Figure 10. Breaking of T_i clamping with up to $T_i \sim 3$ keV achieved in selected experiments. In grey, four configurations show T_i clamping in gas-fueled ECRH plasmas, and dark red triangles represent the neoclassical simulations for the standard configuration, assuming $P_{\text{ECRH}} = 4.5$ MW, as in figure 1. Labelled reference plasmas (labels 1, 2, 2a) and experiments in which the clamping was broken in standard-configuration plasmas (labels 3–5) are: for labels (1), (2) and (2a), power step experiments used in this paper in helium (1) and hydrogen (2) plasmas, respectively (see e.g. figure 11) with a maximum $P_{\text{ECRH}} = 3.9$ MW, and (2a) power steps in a low-density hydrogen plasma (20180906.038) with $P_{\text{ECRH}} = 5, 4, 3.2, 2, 0.7$ MW. (3) Achieved an elevated $T_i \sim 2$ keV in a stationary phase lasting for 40 s, shortly after boronization with a low input power $P_{\text{ECRH}} = 1$ MW (20180808.007, averaged over $t = 8$ –40 s). (4) Transiently achieved $T_i > 2$ keV after dropping boron powder into an ECRH heated plasma with $P_{\text{ECRH}} = 4$ MW (20180927.047, $t = 5.8$ s). (5) Finally, approaching neoclassical values, in which $T_i \sim 3$ keV was transiently achieved during the reheat phase after hydrogen ice-pellet injection with $P_{\text{ECRH}} = 4.5$ MW (20181016.037, $t = 1.7$ s).

at label (2) is shown with $n_{e,0} = 3.5 \times 10^{19} \text{ m}^{-3}$ and a clamped $T_i \sim 1.5$ keV, as in [22].

A stationary elevated $T_{i,0} = 2$ keV was achieved (label (3) in figure 10) above the clamped value, a day after standard boronisation (not a powder-dropper) in a steady-state hydrogen-fueled plasma lasting almost 60 s with low power of $P_{\text{ECRH}} = 1$ MW during the first 40 s and with an averaged density $\langle n_e \rangle = 4 \times 10^{19} \text{ m}^{-3}$. It is suggested that a combination of fresh wall conditioning and low power electron heating helped to increase the normalized density gradient from $a/L_n \sim 0.5$ (e.g. figure 7) to $a/L_n \sim 2$ in the outer plasma region $r/a = 0.5$ –1. The ion temperature may be increased through the mechanism of density-gradient-aided turbulence suppression. It is not understood why, in subsequent pulses with higher $P_{\text{ECRH}} = 4$ MW and similar averaged density, the density gradient in the outer plasma region $r/a > 0.5$ reduced to $a/L_n \sim 0.5$ and subsequently the ion temperature was clamped at $T_{i,0} = 1.5$ keV. Suggested mechanisms that may influence the density profile shape include enhanced wall outgassing by ECRH, causing increased neutral recycling levels, and a possible ‘density pump-out’ caused by central electron heating that reduces the profile peaking.

Transient improvements to higher values of T_i have also been achieved. Here, two examples are shown, representing similar findings in other experiments. First, on the same day as the power step experiments (1) and (2), the first trials with a boron-powder dropper instrument (4) were conducted, in which the central ion temperature rose to $T_{i,0} = 2.3$ keV. The details of the boron-powder experiment and its influence on the kinetic profiles are described in [61]. Basically, the introduced boron helps to reduce the neutral hydrogen source. As a result, the edge density is reduced, while the core density remains unchanged. The resulting enhanced density gradient across the profile helps to suppress the turbulence. Moreover, impurities can stabilize the ITG modes. The reduction of the turbulence may also be due to the increase of impurity density as well as the change of edge density gradient. Unfortunately, shortly after the boron-powder enhanced T_i phase, the ion temperature relaxed back to the pre-boron-powder injection phase $T_i \sim 1.6$ keV. Only after multiple injection phases did the baseline T_i somewhat rise above the clamped value. The price to pay is therefore an increased impurity content, with Z_{eff} rising from 1.3 to 3.2.

The second example, label (5) in figure 10, is a transient increase of the ion temperature after ice-pellet injection to a level well above the clamped level, $T_{i,0} = 3$ keV [8, 9, 23], i.e. close to the maximum achievable T_i according to neoclassical simulations. After a train of pellets is injected, strong density gradients of up to $a/L_n < 3$ are built. After the initial temperature collapse due to the pellet cooling, the ECRH power is increased from 2 to 4.5 MW and during the reheat phase T_i and T_e increase simultaneously and reach $T_{e,0} \sim T_{i,0} = 3$ keV. A detailed PB analysis shows that the ion heat flux at this point is almost fully dominated by neoclassical transport, whereas the electron transport remains largely turbulence dominated. As both the density gradient and the ion root radial electric field rise after the pellet injection, a theoretical analysis using non-linear gyro-kinetic simulations with the GENE code compared the effect of strong density gradients as well as a radial electric field on the turbulent transport. The results show that both can help to reduce the turbulent transport, but that in the case of the pellet experiments, the introduction of a strong density gradient is likely to be the main driving mechanism for the (ITG) turbulence suppression [7]. It is found that simultaneous TEM turbulence is not strongly induced by the enhanced density gradients, and instead, a so-called ion-TEM or iTEM is the dominant mode during the high- T_i phase. Modeling shows that the turbulent ion heat diffusivity is reduced by an order of magnitude compared to the pre-pellet phase, explaining the enhanced ion temperature during this transient phase. Unfortunately, the high confinement phase is terminated on a particle confinement timescale of ~ 100 ms as the density gradients relax back to the pre-pellet conditions.

For future scenario development, a remaining question is whether strong density gradients can be sustained in a stationary fashion. No doubt, the development of scenarios using steep density gradients to sustain high plasma confinement will use up a lot of future machine time at W7-X. A valid question therefore remains: how good a performance can be obtained in standard ECRH plasmas when the

heating capacity is increased to $P_{\text{ECRH}} = 10$ or 15 MW? The ion gyro-Bohm transport simulations in figures 5 and 6 show that the achievable ion temperature would already be saturated under such transport conditions. However, even at the highest density achievable by ECRH-O2 heating, $1.6 \times 10^{20} \text{ m}^{-3}$, the ratio T_e/T_i is not unity (figure 6(c)). A valid transport model would therefore also need to capture the effect of the T_e/T_i ratio on the ITG turbulence.

Acknowledgments

This work has been carried out within the framework of the EUROfusion Consortium and has received funding from the Euratom Research and Training Program 2014–2018 and 2019–2020 under Grant Agreement No. 633053. The views and opinions expressed herein do not necessarily reflect those of the European Commission.

Appendix A. Experimental power balance study

An accurate PB is conducted, in which all the sources and sinks for the heat transport are considered. The experimental heat flux Q_{exp} is the sum of the neoclassical Q_{NC} and the turbulent heat flux Q_{turb} . The steady-state PB, with separate sources and sinks for electrons and ions, is composed of:

$$Q_{e,\text{exp}} = Q_{e,\text{NC}} + Q_{e,\text{turb}} = Q_{\text{ECRH}} - Q_{e-i} - Q_{\text{rad}} \quad (4.1)$$

$$Q_{i,\text{exp}} = Q_{i,\text{NC}} + Q_{i,\text{turb}} = Q_{e-i} - Q_{\text{cx}}, \quad (4.2)$$

where the source Q_{ECRH} is calculated by combining the power-density profiles p_{ECRH} for all ECRH sources using the microwave ray-tracing code Travis [39]. The energy transfer between the electrons and ions Q_{e-i} is a sink for the electrons and a source for the ions, and the power density profile p_{e-i} is calculated from the kinetic profiles using equation (2.1). The radiated heat flux Q_{rad} is the volume-integrated power density profile p_{rad} obtained from a poloidal integration of the tomographic reconstruction of the bolometer multiple lines of sight [47, 48]. Finally, a sink for the ions is the charge exchange loss Q_{cx} between the hot ions and cold neutrals entering the plasma. Although the neutral source is difficult to estimate and forms an uncertain factor in the PB, the effect is only likely to be large near the plasma edge and will not significantly affect the balance at, or inside, the mid radius, as will be shown in this appendix. The neoclassical heat fluxes $Q_{e,\text{NC}}$ and $Q_{i,\text{NC}}$ are calculated with the help of the neoclassical transport solver NTSS, using the experimental profiles as inputs as well as DKES for the transport table. For a description of DKES, see [62, 63]; for its application to W7-X, see [28] and the application of NTSS in [29].

As a target plasma for the PB, an ECRH power step-down experiment in a medium-density hydrogen-fueled plasma is chosen, for which the time traces of the major parameters are shown in figure 11(a). The upper bound of the ECRH

power used in the experiment is limited to 3.9 MW due to the requirement to share the high-voltage power supply between the ECRH system and the NBI system used to provide 10 ms beam blips for the CXRS T_i measurements. The choice of density of $\langle n_e \rangle = 6 \times 10^{19} \text{ m}^{-3}$ is a trade-off between various factors. First, the exchange power density p_{e-i} is maximized at high densities due to its n^2 -dependence, but also has an optimum temperature difference (figure 2). Second, an upper boundary for the density is set by the radiation limit for the lowest ECRH power step to ensure that $P_{\text{ECRH}} < P_{\text{rad}}$. And third, a lower boundary is set to minimize errors in determining the turbulence heatflux $Q_{\text{turb}} = Q_{\text{exp}} - Q_{\text{NC}}$ by avoiding zero crossings of the ambipolar radial electric field E_r , and thus ensuring that E_r is negative across the entire profile (ion root). E_r profile measurements with DR [56] and CXRS [] have confirmed the ion root conditions across the full profile for each power step.

For the hydrogen-fueled plasma, the temperature and density profiles are given in figure 3 for the highest power level $P_{\text{ECRH}} = 3.9$ MW in the scan. The central electron temperature of $T_e = 3$ keV guarantees the optimum energy transfer at an ion temperature of $T_i = 1.5$ keV, (see figure 2). Unfortunately, in the selected hydrogen plasma, the density is too high to conduct a wide ECRH power scan. Already at $P_{\text{ECRH}} = 1.7$ MW, a high radiation front enters the confinement region. This effect is seen in figure 12(a), which shows the radiative power density profile for each power step. For the first two power steps, $P_{\text{ECRH}} = 3.9$ MW and 3.3 MW, most of the power is radiated at $r/a > 0.8$; inside that radius, the volume integral of the radiated power profile is $P_{\text{rad,core}} < 100$ kW. However, at the third power step ($t = 4.5$ – 5.5 s), the radiation moves in to $r/a \sim 0.5$, and the kinetic profiles are strongly affected. Therefore, the selected hydrogen plasma does not meet our requirements.

Helium is considered as an alternative fuel, as helium plasmas have a higher radiative density limit compared to hydrogen plasmas. This is because the wall-impurity sources are reduced due to a lack of chemical sputtering by helium, compared to hydrogen radicals in the divertor. Figure 11(b) shows the waveforms achieved with power steps of 3.9, 2.4, 1.8, and 1.2 MW. Indeed, a plasma with a lower ECRH power down to 1.2 MW can be sustained at an even higher density level, compared to the hydrogen plasma. Figure 12(a) shows that for all power levels, the radiation front stays outside $r/a > 0.8$. Even for the lowest power step, the core radiation for $r/a < 0.8$ is small at $P_{\text{rad,core}} \sim 150$ kW. For the highest power level $P_{\text{ECRH}} = 3.9$ MW, the T_i and T_e profiles as given in figure 15 are similar to that of the H plasma, whereas the electron density is somewhat higher at $\langle n_e \rangle = 7 \times 10^{19} \text{ m}^{-3}$. Also, the plasma performance is similar between the helium- and hydrogen-fueled plasmas with a diamagnetic stored energy for both of $W_{\text{dia}} \approx 0.5$ MJ \pm 0.05 MJ. As a result, the confinement times of both plasmas are virtually identical at $\tau_E = 130$ ms, and despite the small density difference, the ISS04 scaling is also similar at $\tau_{E/\tau_{\text{ISS04}}} \sim 0.65$ for the H and He fueled plasmas. These findings are consistent with the volume integral of the kinetic profiles, as $(n_e + n_i)_{\text{H-fueled}} \approx$

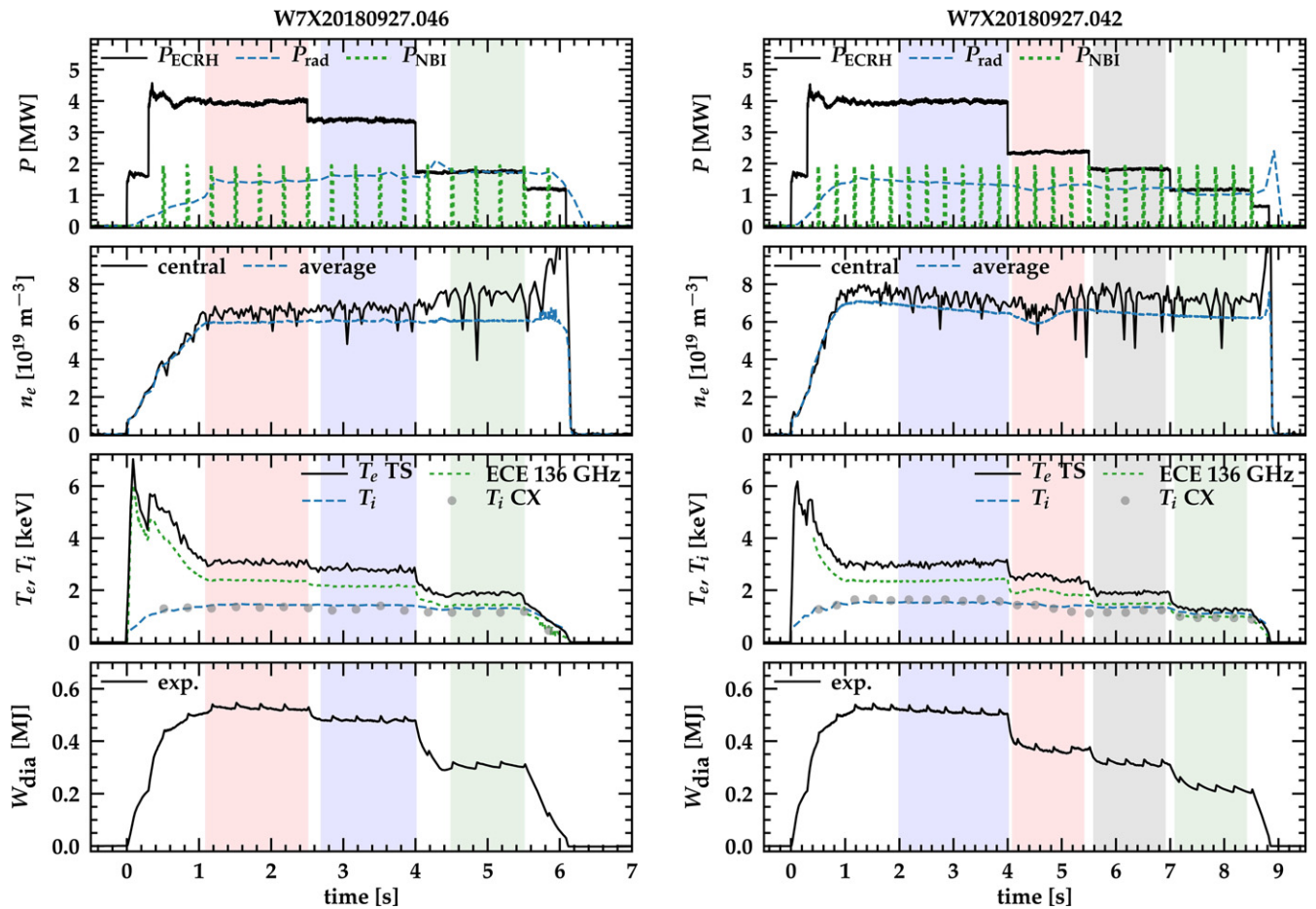


Figure 11. Typical time traces for (left) a hydrogen-fueled plasma and (right) a helium-fueled plasma. Top panel: ECRH heating steps, NBI power blips for CXRS and radiative power. Second panel: central (Thomson) and line-averaged (interferometer) electron densities. Third panel: central T_e (TS and ECE) and central T_i (XICS central chord and CXRS) and bottom panel: diamagnetic stored energy. The colored areas indicate the averaging windows for the profiles and subsequent PB analysis in figures 7 and 15.

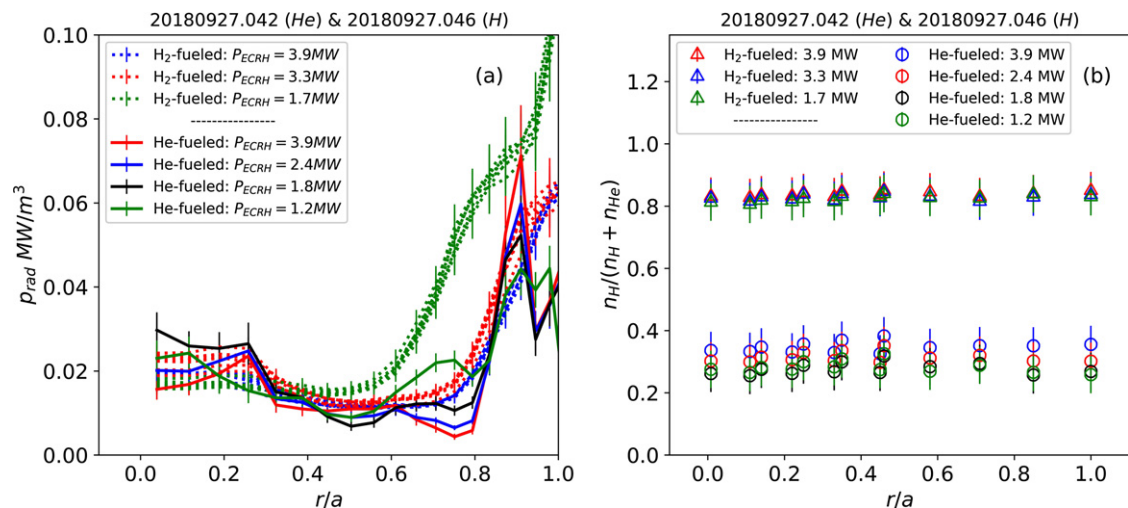


Figure 12. (a) Radiated power density for the H-fueled plasma (dashed) and the He-fueled plasma (solid), for the various ECRH power steps in figure 11. (b) Concentration of hydrogen with respect to helium in the H-fueled plasma (triangles) and the He-fueled plasma (circles) respectively.

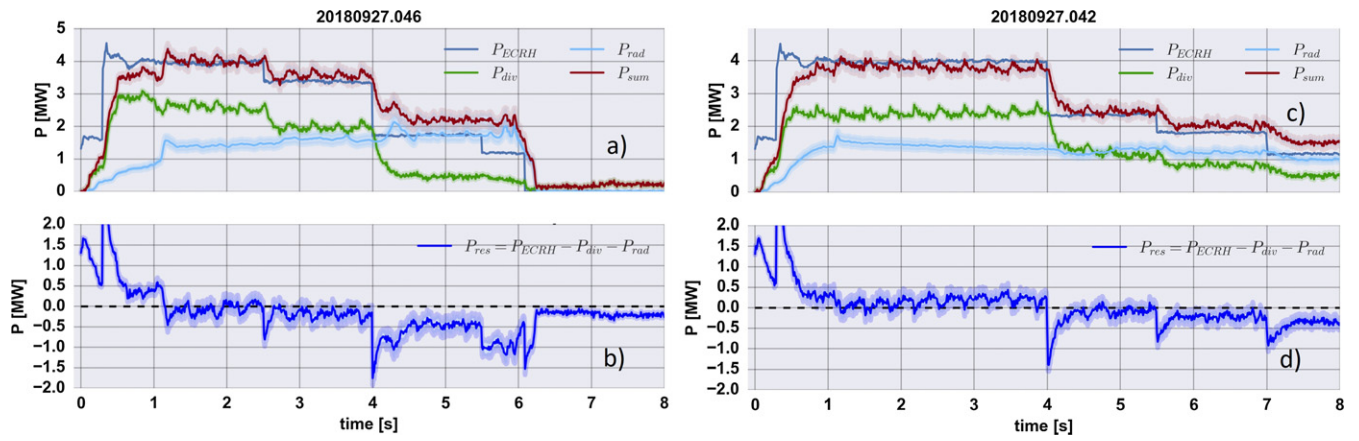


Figure 13. Divertor PB $P_{\text{res}} = P_{\text{ECRH}} - P_{\text{div}} - P_{\text{rad}}$ for (a) the hydrogen-fueled #20180927.046 and (c) helium-fueled plasma #20180927.042 (right). The divertor heat load P_{div} is reconstructed from IR thermography camera data integrated over all five double-divertor modules [17]. The radiated power P_{rad} is taken from a poloidal averaged polarimeter-tomographic reconstruction and assumes toroidal symmetry. (b) and (d) The residual P_{res} is balanced within ~ 200 kW for the phases in which $P_{\text{rad}} < P_{\text{ECRH}}$ up to the time point $t = 7$ s.

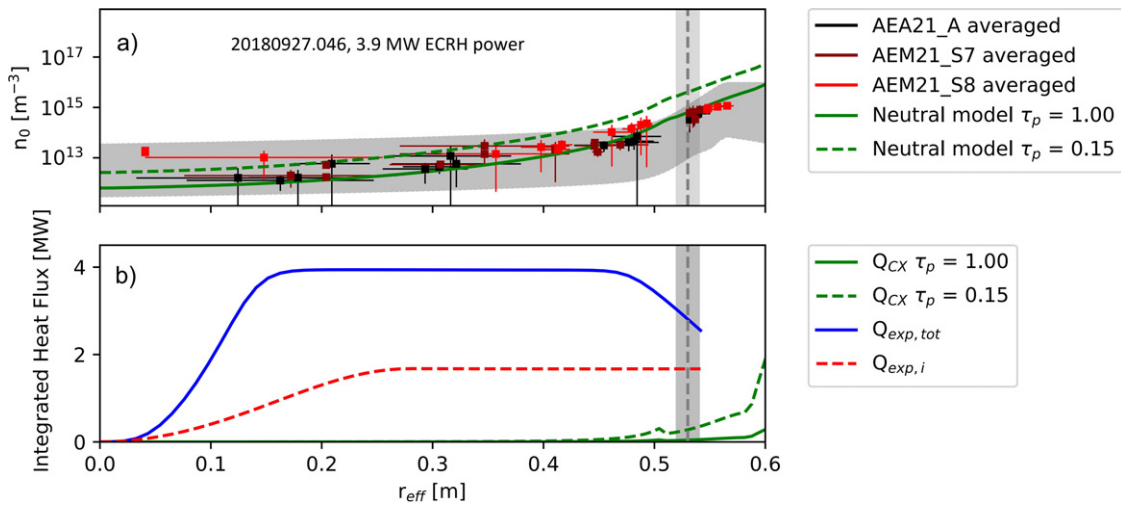


Figure 14. (a) Neutral density as derived from H_{α} spectroscopy from three different lines of sight of the CXRS diagnostic [45] (AEA21_A is a pure toroidal line of sight, and AEM21_S7 and AEM21_S8 are half poloidal, half toroidal lines of sight). The grey shaded areas are not errors, but rather an assessment with a lower and upper bound for the neutral density; the lower bound of this band is obtained by equating ionization and recombination using ADAS coefficients [66]. As this relates to the case of no inward neutral transport, this approach gives a lower limit for the neutral density. The upper limit is obtained by assuming that the neutral density pressure stays constant over the plasma. It is normalized using the edge data points and propagated inwards using the ion temperature from the XICS system (figure 7(a)). As the neutral pressure should, at most, be constant, this gives an upper bound. The error bars for the data are given as vertical and horizontal lines for each data point. The measured profile of n_0 is compared to a neutral model with a variation of the particle confinement time from $\tau_p = 150$ ms to $\tau_p = 1$ s. (b) The estimated charge exchange losses Q_{CX} (from $\tau_p = 150$ ms to $\tau_p = 1$ s) compared to the experimental total heat flux $Q_{\text{exp,tot}}$ and $Q_{\text{exp,i}}$ from figures 7(d) and (e), respectively. The vertical dashed line represents the separatrix position.

$(n_e + n_i)_{\text{He-fueled}}$; they yield a thermal stored energy in both plasmas of $W_{\text{th}} = 0.52 \pm 0.04$ MJ.

Since a wider ECRH power range is possible in the helium-fueled plasma, the power steps in this plasma are used to study the temperature-clamping phenomenon, while a comparison of the H and He plasmas at $\text{PECRH} = 3.9$ MW is used to link to the wider post-boronization hydrogen W7-X database in figure 1.

Neither of the plasmas discussed is a pure single-species plasma, but contains a fuel mix of H and He. Figure 12(b) shows the ratio $R_{\text{H/H+He}} = n_{\text{H}}/(n_{\text{H}} + n_{\text{He}})$ derived from

charge exchange spectroscopy; for the H-fueled plasma, $R_{\text{H/H+He}} = 85\%$, and for the He-fueled plasma, $R_{\text{H/H+He}} = 25\% - 30\%$. In fact, to get pure single-species plasmas is time consuming in W7-X. The reason for this is that, on the one hand, the helium is not fully pumped in W7-X. Since the H-fueled plasma was preceded by He-fueled plasmas, a H/He mix is the consequence. On the other hand, and vice versa, due to the high hydrogen retention of the carbon plasma-facing components, H outgassing in a He-fueled plasma is relatively high if the previous plasmas contained H as a fuel. In the current conditions, high helium fuel purity can only be achieved

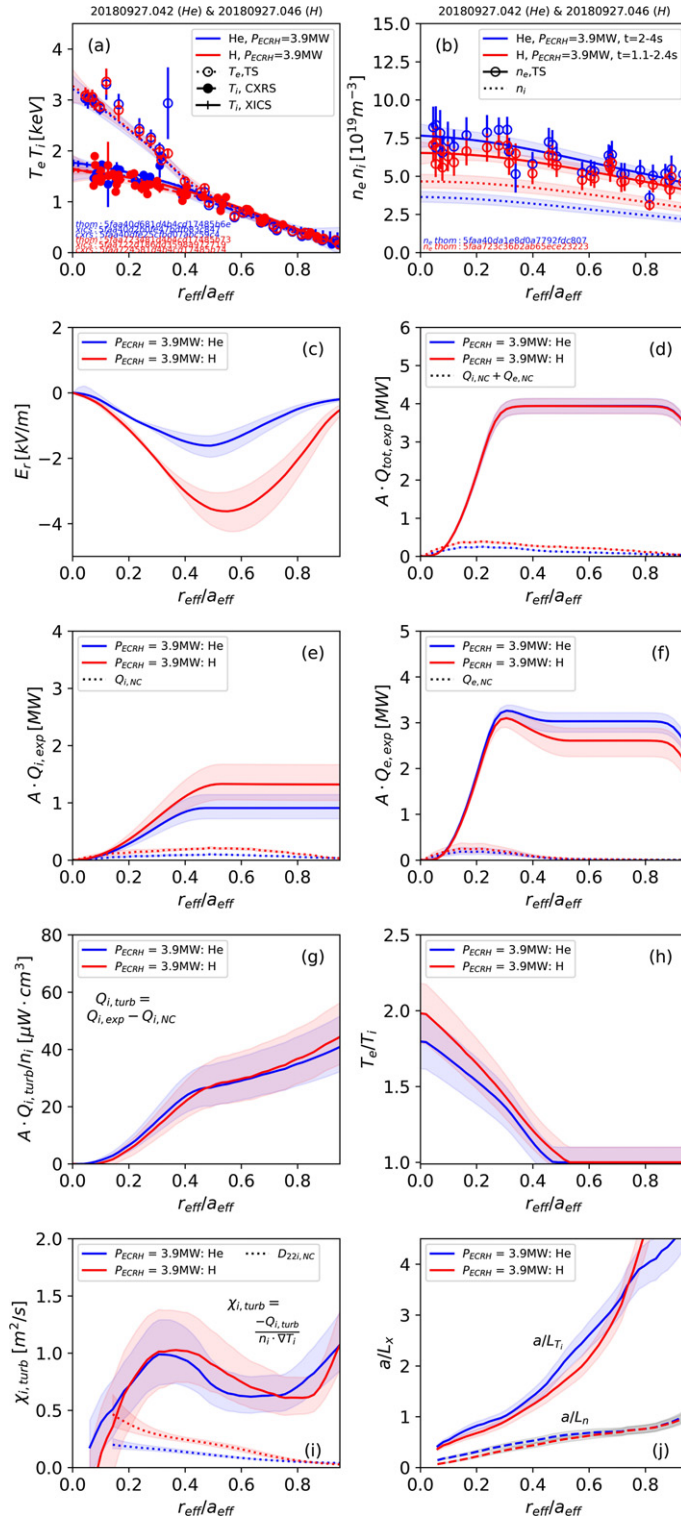


Figure 15. Profile comparison of H- (red) vs He- (blue) fueled plasmas: (a) T_e using TS and T_i measured by XICS and CXRS; (b) the density, n_e , using TS and n_i from line-averaged $Z_{\text{eff}} \sim 1.4$ and $Z_{\text{eff}} \sim 2$, assuming only a H vs He mixture. (c) Ambipolar radial electric field E_r . (d) Total experimental volume-integrated heat flux $A \cdot Q_{\text{tot,exp}}$ (solid) compared to the total neoclassical integrated heat flux $A \cdot Q_{\text{tot,NC}}$ (dashed), (A is the flux surface area). (e) Experimental volume-integrated ion heat flux $A \cdot Q_{i,\text{exp}}$ (solid) as calculated from the exchange power, compared to the neoclassical integrated ion heat flux $A \cdot Q_{i,\text{NC}}$ (dashed). (f) Experimental volume-integrated electron heat flux $A \cdot Q_{e,\text{exp}}$ (solid) compared to the neoclassical integrated electron heat flux $A \cdot Q_{e,\text{NC}}$ (dashed). (g) Volume-integrated turbulent ion heat flux normalized to the ion density $A \cdot Q_{i,\text{turb}}/n_i$. (h) Profiles of T_e/T_i (i) turbulence ion heat diffusivity— A is the flux surface area; (j) normalized ion temperature gradient a/L_{T_i} and density gradient length a/L_n where $L_x = x/\nabla x$.

after a time-consuming wall-conditioning program with repetitive pulses, for which no experimental time was allocated. (Note for reference that outside of this experimental day, only hydrogen plasmas are run and high hydrogen-fuel purity is usually obtained)

For the core PB coming up in the next section we derive the ion density profile in the H/He fuel mixes from figure 12(b) as $n_i/n_e = 0.9$ and $n_i/n_e = 0.65$, respectively. Note that the $R_{H/H+He}$ profiles are flat for both plasmas and almost constant throughout the ECRH power steps. If we assume no other species than H and He are present in the plasma, then $n_i/n_e = (z_{He} + 1)/z_{He} - Z_{eff}/z_{He}$, and we derive $Z_{eff} = 1.3$ and $Z_{eff} = 1.8$, respectively. These values are consistent with the Z_{eff} values obtained from bremsstrahlung spectroscopy.

Finally, the charge exchange losses are estimated. First, a divertor PB is considered, as seen in figure 13. The total power that arrives at the divertor tiles P_{div} as measured by infrared (IR) thermography [64] is compared to the total ECRH power as well as the total radiated power P_{rad} . The latter is reconstructed from bolometer tomography [47] by assuming toroidal symmetry. The residual (or unaccounted-for) power is given by $P_{res} = P_{ECRH} - P_{div} - P_{rad}$. Figure 13 shows that this residual power is of the order of 100–200 kW for both hydrogen- and helium-fueled plasmas, which is the uncertainty margin of the divertor PB. Only when the relative plasma radiation increases, such that $P_{rad} \sim P_{ECRH}$, does the apparent discrepancy increase above this range, albeit the symmetry assumption of P_{rad} may no longer be valid. As a result the non-absorbed charge exchange losses for the phases in which $P_{rad} < P_{ECRH}$ may be, at most, of the order of $P_{CX} \sim P_{res} \sim 100\text{--}200$ kW.

The local charge exchange losses are furthermore estimated from the neutral particle density profile for the hydrogen-fueled plasma (figure 14). The reconstruction follows the methodology described in [65], using multiple passive H_α lines of sight of the CXRS diagnostic [45] and assuming poloidal symmetry. No inversion is required, as multiple measurements are localized along each single line of sight using the Doppler broadening of multiple spectral components, which are subsequently related to the main ion temperature profile. Full details of the method are given in [65]. Depending on the particle confinement time assumed in the estimation, the charge exchange losses Q_{CX} are of the order of 10–100 kW at the separatrix, and further inside, at $r/a \sim 0.8$ ($r_{eff} \sim 0.4$ m), Q_{CX} is estimated to be negligibly small compared to the total and ion heat fluxes Q_{exp} and $Q_{i,exp}$ (from figures 7(d) and (e)). We therefore ignore the charge exchange losses in the further core PB analysis.

We now come to the PB analysis and the comparison of the helium- and hydrogen-fueled plasmas (figure 15). Figure 15(c) shows the profiles of the ambipolar radial electric field E_r as calculated by the NTSS code. As both plasmas feature ion-root transport with negative E_r , the errors in $Q_{i,NC}$ and $Q_{e,NC}$ around root transitions are avoided. The experimental heat fluxes are shown in figures 15(d)–(f) for the sum of the electron and ion fluxes, the electrons, and the ions, respectively. As a comparison, the neoclassical fluxes are also shown using dashed lines. Clearly, the turbulence heat flux dominates across the profile

for $r/a > 0.1$, showing that the turbulent transport determines the energy confinement. Not shown in figure 15 are the radiative losses (figure 12(b)), which are already accounted for in $Q_{e,exp}$ and are negligible compared to Q_{ECRH} and Q_{e-i} up to a radius of $r/a \sim 0.8$. The charge exchange Q_{CX} loss channel for the ions can be neglected in the analysis. The ion heat flux in figure 15(e) is higher in the hydrogen-fueled case, due to the Z/M dependency of p_{e-i} (equation (2.1)). However as the ion density is lower in the helium-fueled plasmas, the normalized ion heat fluxes $Q_{i,turb}/n_i$ are virtually the same in the hydrogen- and helium-fueled plasmas, figure 15(g). Therefore, as the kinetic profiles and their gradients (figure 15(j)) look similar for the two plasmas, the ion heat diffusivity for the hydrogen- and helium-fueled plasmas are also similar (figure 15(i)) and is of the order of $0.5\text{--}1$ m² s⁻¹ across the full profiles, i.e. well above the neoclassical diffusivity $D_{22,i}$. We therefore conclude from this PB comparison that no significant difference is observed in the ion heat transport between the H- and He-fueled plasmas. For this reason, we are justified in using the helium-fueled plasma in the ion transport study to probe the ion profile stiffness.

ORCID iDs

M.N.A. Beurskens  <https://orcid.org/0000-0002-3354-0279>
 S.A. Bozhakov  <https://orcid.org/0000-0003-4289-3532>
 P. Xanthopoulos  <https://orcid.org/0000-0003-3545-4822>
 A. Zocco  <https://orcid.org/0000-0003-2617-3658>
 A. Alonso  <https://orcid.org/0000-0001-6863-8578>
 C. Beidler  <https://orcid.org/0000-0002-4395-239X>
 D. Carralero  <https://orcid.org/0000-0002-7824-3307>
 T. Estrada  <https://orcid.org/0000-0001-6205-2658>
 K. Ida  <https://orcid.org/0000-0002-0585-4561>
 M. Jakubowski  <https://orcid.org/0000-0002-6557-3497>
 C. Killer  <https://orcid.org/0000-0001-7747-3066>
 S. Kwak  <https://orcid.org/0000-0001-7874-7575>
 S. Lazerson  <https://orcid.org/0000-0001-8002-0121>
 A. Langenberg  <https://orcid.org/0000-0002-2107-5488>
 R. Lunsford  <https://orcid.org/0000-0003-3588-6801>
 N. Pablant  <https://orcid.org/0000-0001-6617-8459>
 A. Pavone  <https://orcid.org/0000-0003-2398-966X>
 Th. Romba  <https://orcid.org/0000-0002-2727-9385>
 D. Zhang  <https://orcid.org/0000-0002-5800-4907>
 R.C. Wolf  <https://orcid.org/0000-0002-2606-5289>

References

- [1] Pedersen T.-S. et al 2019 *Plasma Phys. Control. Fusion* **61** 014035
- [2] Wolf R.C. et al 2019 *Phys. Plasmas* **26** 082504
- [3] Klinger T. et al 2019 *Nucl. Fusion* **59** 112004
- [4] Maaßberg H., Beidler C.D. and Simmet E.E. 1999 *Plasma Phys. Control. Fusion* **41** 1135–53
- [5] Nührenberg J. and Zille R. 1986 Stable stellarators with medium β and aspect ratio *Phys. Lett. A* **114** 129–32
- [6] Alcusón J.A., Xanthopoulos P., Plunk G.G., Helander P., Wilms F., Turkin Y., Stechow A.v. and Grulke O. 2020 *Plasma Phys. Control. Fusion* **62** 035005

- [7] Xanthopoulos P. *et al* 2020 *Phys. Rev. Lett.* **125** 075001
- [8] Bozhnikov S.A. *et al* 2020 *Nucl. Fusion* **60** 066011
- [9] Baldzuhn J *et al* 2020 *Plasma Phys. Control. Fusion* **62** 055012
- [10] Beidler C.D. *et al* 2021 Demonstration of reduced neoclassical energy transport in Wendelstein 7-X *Nature* **596** 221–6
- [11] Smith H. *et al* 2019 “Would the Wendelstein 7-X ”Record Discharge” Have Been Possible in Other Magnetic Configurations?” 22nd International Stellarator & Heliotron Workshop 23 – 27 september 2019 Madison, WI, USA
- [12] Yamada H. *et al* 2005 *Nucl. Fusion* **45** 1684–93
- [13] Dinklage A. *et al* 2007 *Nucl. Fusion* **47** 1265–73
- [14] Fuchert G. *et al* 2020 *Nucl. Fusion* **60** 036020
- [15] Wauters T. *et al* 2018 *Nucl. Mater. Energy* **17** 235–41
- [16] Schmitz O. *et al* 2021 *Nucl. Fusion* **61** 016026
- [17] Jakubowski M. *et al* 2021 *Nucl. Fusion* **61** 106003
- [18] Grulke O. *et al* (“Wendelstein 7-X: Towards high-density, long-pulse operation”, 46th Conference on Plasma Physics (EPS), 8–12 July 2019, Milan, Italy)
- [19] Beidler C.D., Feng Y., Geiger J., Köchl F., Maaßberg H., Marushchenko N.B., Nührenberg C., Smith H.M. and Turkin Y. 2018 *Plasma Phys. Control. Fusion* **60** 105008
- [20] Langenberg A. *et al* 2020 *Phys. Plasmas* **27** 052510
- [21] Geiger B. *et al* 2019 *Nucl. Fusion* **59** 046009
- [22] Wegner T. *et al* 2020 *Nucl. Fusion* **60** 124004
- [23] Jenko F., Dorland W., Kotschenreuther M. and Rogers B.N. 2000 *Phys. Plasmas* **7** 1904
- [24] Hirsch M. *et al* 2017 *Nucl. Fusion* **57** 086010
- [25] Pablant N.A. *et al* 2018 *Phys. Plasmas* **25** 022508
- [26] Dinklage A. *et al* (the W7-X Team) 2018 *Nat. Phys.* **14** 855–60
- [27] Weir G.M. *et al* 2021 *Nucl. Fusion* **61** 056001
- [28] Turkin Y., Maassberg H., Beidler C.D., Geiger J. and Marushchenko N.B. 2006 Current control by ECCD for W7-X *Fusion Sci. Technol.* **50** 387–94
- [29] Turkin Y., Beidler C.D., Maaßberg H., Murakami S., Tribaldos V. and Wakasa A. 2011 *Phys. Plasmas* **18** 022505
- [30] Wesson J. 2003 *Tokamaks* (Oxford: Clarendon)
- [31] Wolf R.C. *et al* 2019 *Plasma Phys. Control. Fusion* **61** 014037
- [32] Beurskens M.N.A. (JET-EFDA Contributors) 2013 *Nucl. Fusion* **53** 013001
- [33] Beurskens M.N.A. *et al* 2013 *Plasma Phys. Control. Fusion* **55** 124043
- [34] Beurskens M.N.A. *et al* 2014 *Nucl. Fusion* **54** 043001
- [35] Pasch E., Beurskens M.N.A., Bozhnikov S.A., Fuchert G., Knauer J. and Wolf R.C. 2016 *Rev. Sci. Instrum.* **87** 11E729
- [36] Bozhnikov S.A. *et al* 2017 *J. Inst.* **12** P10004
- [37] Hirsch M. *et al* 2019 ECE diagnostic for the initial operation of Wendelstein 7-X *EPJ Web Conf.* **203** 03007
- [38] Hoefel U. *et al* 2019 Bayesian modeling of microwave radiometer calibration on the example of the Wendelstein 7-X electron cyclotron emission diagnostic *Rev. Sci. Instrum.* **90** 043502
- [39] Marushchenko N.B., Turkin Y. and Maassberg H. 2014 Ray-tracing code TRAVIS for ECR heating, EC current drive and ECE diagnostic *Comput. Phys. Commun.* **185** 165–76
- [40] Hirshman S.P. and Whitson J.C. 1983 Steepest-descent moment method for three-dimensional magnetohydrodynamic equilibria *Phys. Fluids* **26** 3553–68
- [41] Brunner K.J. *et al* 2018 Real-time dispersion interferometry for density feedback in fusion devices *J. Inst.* **13** P09002
- [42] Pablant N.A. *et al* 2018 Core radial electric field and transport in Wendelstein 7-X plasmas *Phys. Plasmas* **25** 022508
- [43] Kring J. *et al* 2018 *In situ* wavelength calibration system for the x-ray imaging crystal spectrometer (XICS) on W7-X *Rev. Sci. Instrum.* **89** 10F107
- [44] Langenberg A., Svensson J., Thomsen H., Marchuk O., Pablant N.A., Burhenn R. and Wolf R.C. 2016 *Fusion Sci. Technol.* **69** 560–7
- [45] Ford O.P. *et al* (W7-X Team) 2020 *Rev. Sci. Instrum.* **91** 023507
- [46] Cleveland William Swain 2000 STATA: Lowess smoothing (<https://stata.com/manuals13/rlowess.pdf>)
- [47] Zhang D. *et al* 2019 *Phys. Rev. Lett.* **123** 025002
- [48] Zhang D. *et al* 2021 NF “Plasma radiation behavior approaching high-radiation scenarios in W7-X”, Nuclear Fusion, accepted for publication
- [49] Garbet X. *et al* (the JET EFDA Contributors) 2004 *Plasma Phys. Control. Fusion* **46** 1351
- [50] Garbet X. *et al* 2004 *Plasma Phys. Control. Fusion* **46** B557
- [51] Garbet X. *et al* (the JET EFDA Contributors) 2005 *Plasma Phys. Control. Fusion* **47** 957
- [52] Ryter F. *et al* 2001 *Plasma Phys. Control. Fusion* **43** 323A–38
- [53] Ryter F. *et al* 2011 *Nucl. Fusion* **51** 113016
- [54] Ryter F. *et al* 2019 *Nucl. Fusion* **59** 096052
- [55] Zocco A. 2018 *J. Plasma Phys.* **84** 715840101
- [56] Estrada T. *et al* (the W7-X team) 2021 *Nucl. Fusion* **61** 046008
- [57] Xanthopoulos P. *et al* 2014 *Phys. Rev. Lett.* **113** 155001
- [58] Dimits A.M. *et al* 2000 *Phys. Plasmas* **7** 969
- [59] Kinsey J.E., Staebler G.M. and Waltz R.E. 2008 *Phys. Plasmas* **15** 055908
- [60] Warmer F., Xanthopoulos P., Proll J.H.E., Beidler C.D., Turkin Y. and Wolf R.C. 2018 *Nucl. Fusion* **58** 016017
- [61] Lunsford R *et al* 2021 *Physics of Plasmas* **28** 082506
- [62] Hirshman S.P., Shaing K.C., van Rij W.I., Beasley C.O. and Crume E.C. 1986 *Phys. Fluids* **29** 2951
- [63] van Rij W.I. and Hirshman S.P. 1989 *Phys. Fluids B* **1** 563
- [64] Jakubowski M. *et al* 2018 *Rev. Sci. Instrum.* **89** 10E116
- [65] Fujii K., Goto M. and Morita S. 2015 *Nucl. Fusion* **55** 063029
- [66] Summers H.P. and O’Mullane M.G. 2011 *AIP Conf. Proc.* **1344** 179